2D temperature map acquisition using HyperSpectral Imaging System (HSIS)

A Thesis Presented for the
Master of Science
Degree
The University of Tennessee, Knoxville

Anthony Kim
August 2024

ACKNOWLEDGEMENTS

Pursuing my master's degree at the University of Tennessee, Knoxville (UTK) has been a privilege and a remarkable experience to be proactive in my dreams and goals and grow physically, mentally, and spiritually.

I thank God for letting me complete this journey. Whenever I was struggling because of my weakness, he gave me strength and power to withstand and grow. Without Him, I could not have done this. His steadfast and everlasting love was overflowing in my life and allowed me to meet great and kind people who had a significant impact on my life.

First, I acknowledge and thank my advisor Dr. Zhili Zhang, who provided me with the opportunity to come to UTK and have hands-on experience in research. He gave me crucial advice on how to be a good researcher and was patient and generous. I will always keep in mind the things I learned from him and utilize them for my future career.

Second, I want to express gratitude to Dr. Cary Smith, who helped me out with the projects I was on. It was a great pleasure to see him on a weekly basis and have a conversation remotely about the direction and details of the project. I learned how to efficiently communicate with people and how to deal with engineering problems from him. The discussions kept me motivated to carry on the projects.

Also, I would like to thank Dr. Mark Gragston, Dr. Phil Kreth, and Dr. Damiano Baccarella for being my committee members.

Next, I want to thank my parents Jeongguk Kim and Hyosun Park for showing love and support. The encouragement they gave me during this difficult time was essential in gaining momentum and perseverance. Also, it is a great honor to do my graduate studies at the same school where my father did his Ph.D. and to follow his path.

Additionally, I want to thank Alek for helping me with my experiments. Using a laser to run experiments was dangerous but I was able to totally focus on the experiment without anxiety because he always made sure that I was safe during experiments. The politeness he showed and the knowledge he shared will be remembered throughout my life.

Last, I want to thank Camden and Jacob for being my friends with whom I can talk and take classes together. The things we did in Knoxville will be cherished. I will never forget the good memories we shared together.

ABSTRACT

Imaging techniques are close to our lives and are used for various applications. In the engineering field, one of the dominant techniques is hyperspectral imaging. It is a necessary tool that combines spectroscopy and digital photography and provides additional information on what is imaged by the imaging system. Hyperspectral imaging has been applied to various fields including remote sensing, cultural relic conservation, food microbiology, forensic science, biomedicine, etc.

In particular, work was done to apply hyperspectral imaging to measure the temperature and emissivity of an object. Due to its ability to measure temperature and emissivity without being in contact with the material surface, hyperspectral imaging has been regarded as a convenient method to monitor real-time data.

In this research, a HyperSpectral Imaging System (HSIS) is designed to image an object. The Compressed Hyperspectral Augmented Image Reconstruction (CHAIR) algorithm was used to reconstruct the spatial and spectral data, and experiments were designed and carried out to acquire the required inputs of the algorithm. After the essential inputs were obtained, Planck’s law was applied to calculate the temperature of every pixel of the recovered hyperspectral image, and finally, a 2D temperature map was acquired.

TABLE OF CONTENTS

LIST OF TABLES

LIST OF FIGURES

CHAPTER ONE
INTRODUCTION AND RESEARCH OBJECTIVE

Thermal Radiation

In radiation heat transfer, no matter is needed, and the radiated energy is distributed differently over a single spectrum region. To thoroughly understand radiation, one should consider the radiation wavelength and in what direction the radiation is distributed. The electromagnetic wave theory and the quantum theory of photons describe how radiative energy is emitted, absorbed, and transferred. The two theories complement each other and perfectly explain thermal radiation [1].

The quantum theory states that photons (light particles) have no rest mass transfer energy by moving at the speed of light. Each photon transports the energy quantum. The energy transferred by the photon can be written as Equation (1.1).

$$e_{Ph} = h\nu \tag{1.1}$$

where h is the Planck constant ($h = 6.62606896 \pm 0.00000033) \cdot 10^{-34}\, Js$) also referred to as Planck's action quantum, ν is the frequency of the photons. Quantum theory is essential to calculate the spectral distribution of the energy emitted by a body.

According to electromagnetic wave theory, the relationship between the two parameters wavelength λ and frequency ν is shown by Equation (1.2).

$$\lambda \cdot \nu = c \tag{1.2}$$

where c is the speed of light in a medium which is lower than the speed of light in a vacuum ($c_0 = 299792458\, m/s$), ν is the frequency of the photons which remains the same and λ is the wavelength. The electromagnetic waves oscillate perpendicular to the direction of propagation (transverse waves), and the energy transported by the electromagnetic waves depends on λ. Figure 1.1 shows the range of the electromagnetic spectrum. Thermal radiation is within the wavelength range starting from 0.1 μm to 1,000 μm. Bodies within this range that have a temperature range of a few Kelvins and $2 \cdot 10^4$ K radiate. The thermal radiation region is in the visible light region between 0.38 μm

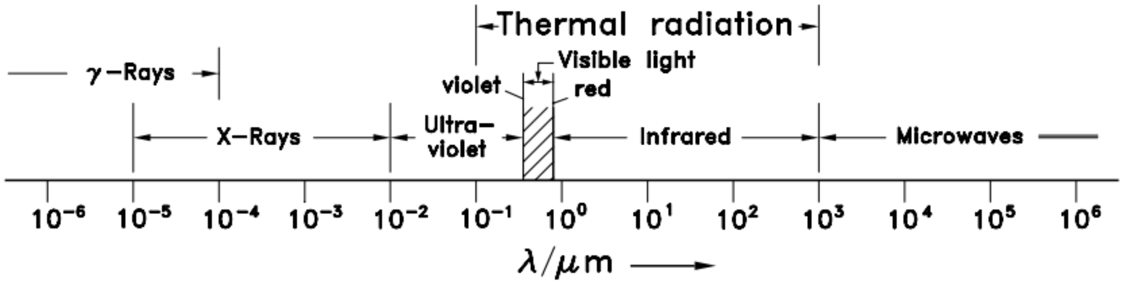

Figure 1.1 Electromagnetic wave spectrum [1].

(violet) and 0.78 μm (red).

Based on the direction, there are directional spectral quantities, hemispherical spectral quantities, directional total quantities, and hemispherical total quantities. Directional spectral quantities explain the directional and wavelength distribution of the radiative energy in depth. Since it is very hard to determine it experimentally or theoretically, radiation quantities that only include either the dependence on the wavelength or the direction are used. Next, the hemispherical spectral quantities average the radiation into all directions of the hemisphere over a surface element and are only dependent on the wavelength. The directional total quantities only describe the dependence on the directions by averaging the radiation over all wavelengths. Lastly, the hemispherical total quantities combine the radiation over all wavelengths and from all directions.

1.1 Radiation from a Blackbody and Planck's Law

A blackbody is defined as a body that completely absorbs and emits incident radiation of all wavelengths and angles. The spectral intensity $L_{\lambda s}(\lambda, T)$ of a blackbody is a universal function of the wavelength and the thermodynamic temperature. Equation (1.3) shows the relationship between the hemispherical spectral emissive power $M_{\lambda s}(\lambda, T)$ and the Kirchhoff's function $L_{\lambda s}(\lambda, T)$.

$$M(\lambda, T) = \pi L_{\lambda s}(\lambda, T) \tag{1.3}$$

In 1900, M. Planck first found Planck's Law and experimentally figured out the details of the universal functions $L_{\lambda s}(\lambda, T)$ or $M_{\lambda s}(\lambda, T)$. The foundations of quantum theory were formed by Planck's law. Planck's law explains the spectral intensity of electromagnetic radiation emitted by a blackbody. It is shown in Equation (1.4).

$$M_{\lambda s}(\lambda, T) = \pi L_{\lambda s}(\lambda, T) = \frac{2\pi h c^2}{\lambda^5 \left(e^{\frac{hc}{\lambda K_B T}} - 1\right)} \tag{1.4}$$

where $L_{\lambda s}(\lambda, T)$ is the spectral radiation intensity of the blackbody, h is the Planck constant ($h = 6.62606896 \pm 0.00000033) \cdot 10^{-34}\ Js$), c is the speed of light in a vacuum ($c \cong 3 \times 10^8$), λ is the wavelength of the radiation, K_B is the Boltzmann's constant (K_B = 1.38 $\times$ $10^{-23} J/K$), and T represents the absolute temperature of the blackbody (K). Figure 1.2 shows $M_{\lambda s}(\lambda, T)$ for several isotherms and Figure 1.3 shows $M_{\lambda s}(\lambda, T)$ in a logarithmic scale.

1.2 Hemispherical Spectral Emissivity and Real Bodies

Kirchhoff's law states that a blackbody emits the maximum radiation energy at every wavelength in every direction in the hemisphere. However, when it comes to real bodies, the directional dependence and the spectral distribution of the radiated energy are different from the properties of a blackbody. Emissivity can be used to explain this characteristic. Equation (1.5) shows the hemispherical spectral emissivity which gives the spectral energy distribution.

$$\varepsilon_\lambda(\lambda, T) = \frac{M_\lambda(\lambda, T)}{M_{\lambda s}(\lambda, T)} = \frac{L_\lambda(\lambda, T)}{L_{\lambda s}(\lambda, T)} \tag{1.5}$$

where $\varepsilon_\lambda(\lambda, T)$ describes the wavelength distribution of the radiative power emitted in the hemisphere by comparing the hemispherical spectral emissive power $M_\lambda(\lambda, T)$ with that of a blackbody $M_{\lambda s}(\lambda, T)$. Hemispherical spectral emissivity ranges between 0 and 1 depending on the temperature and wavelength.

Real bodies can be explained whether the emissivity depends on the wavelength. A graybody is an object that has an invariant emissivity with changing wavelength. On the other hand, if the emissivity depends on the wavelength, the object is called a non-graybody. The spectral emissivity and spectral radiant flux for blackbody, graybody, and non-graybody are shown in Figure 1.4.

Research Objectives

The objectives of this work are to have a thorough understanding of the Compressed Hyperspectral Augmented Image Reconstruction (CHAIR) algorithm to reconstruct the spatial (x,y) and spectral (λ) data, to improve the spatial reconstruction by determining the optimized sparsity (values of pixels per inch and dot concentration) of the binary pattern, to design an experimental setup with a red and green laser to demonstrate the

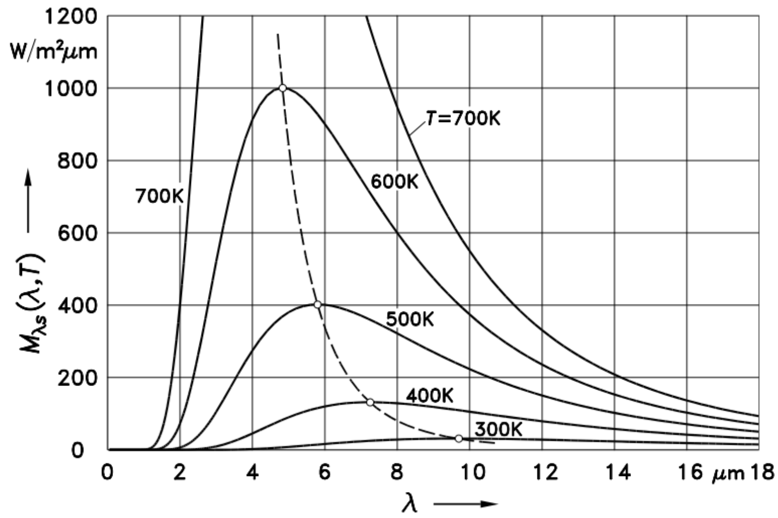

Figure 1.2 The hemispherical spectral emissive power of a black body according to Planck's radiation law [1].

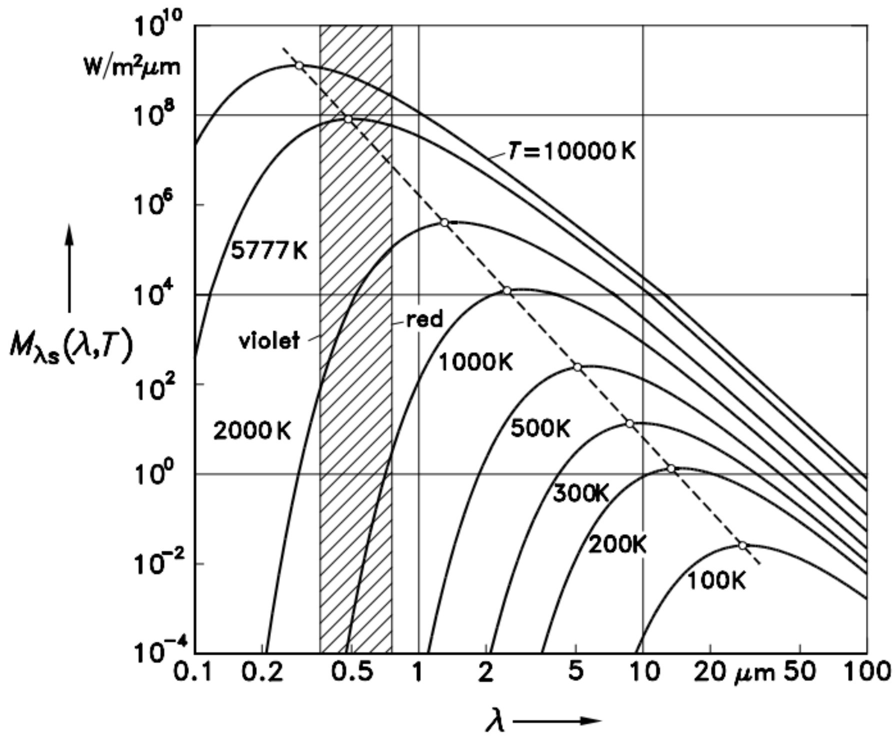

Figure 1.3 The hemispherical spectral emissive power in a logarithmic scale [1].

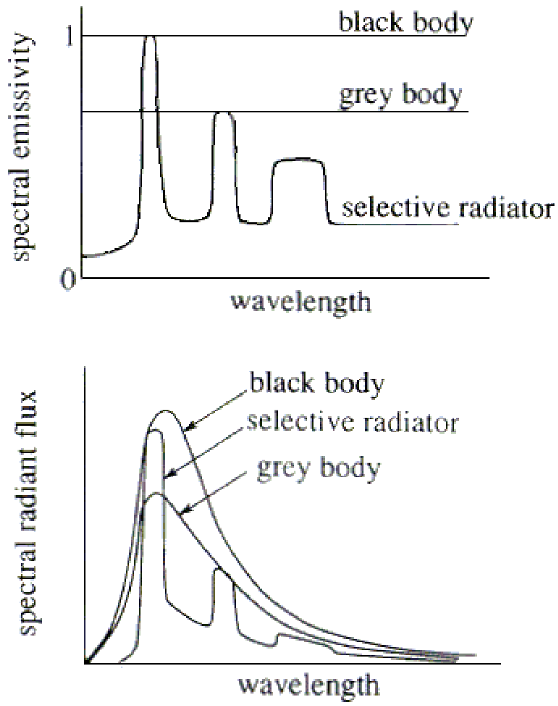

Figure 1.4 The spectral emissivity and spectral radiant flux for blackbody, graybody, and non-graybody [1].

concept of the CHAIR algorithm, to use the imaging system to acquire the ground truth spectrum of a graphite plate heated to 1,020 ℃, and to acquire a two-dimensional temperature map by correlating the reconstructed data, Planck's law, and emissivity. More details are going to be presented in the following chapters.

CHAPTER TWO LITERATURE REVIEW

Overview of Hyperspectral Imaging

2.1 History and Application of Hyperspectral Imaging

Hyperspectral Imaging, also known as imaging spectrometry, was developed by NASA's Jet Propulsion Laboratory in the late 1970s. Hyperspectral imaging (imaging spectrometry) was defined as the simultaneous acquisition of images in many narrow, contiguous spectral bands in such a way that a continuous reflectance spectrum can be reconstructed for each picture element (pixel) in the scene [2]. This concept is shown in Figure 2.1. Back then, it was attempted to apply this new approach to remote sensing and the typical spectral region was 0.4 to 2.5 μm with a sampling interval of 10 nm. To accomplish this, the Landsat Multispectral Scanner (MSS) [3] or Thematic Mapper (TM) [4] were needed because of their low spectral resolution.

As the technologies that are relevant to hyperspectral imaging developed, hyperspectral imaging started to be applied in various fields [5] including cultural relic conservation [6,7], food microbiology [8], forensic science [9], and biomedicine [10], etc. Figure 2.2 shows a schematic of how relic conservation is done using hyperspectral imaging. By taking a hyperspectral image of a painting, mural, or porcelain and looking at a certain pixel of the hyperspectral image, the pixel of a reflectance curve versus the wavelength can be easily obtained [7], and the details of the object will be gained since the reflectance variation of the object along with the wavelength variation is dominantly determined by the physical properties of the matter. The high resolution and broad wavelength range of hyperspectral imaging will substantially improve data processing and analysis efficiency. Also, for the past two decades, miscellaneous hyperspectral imaging systems have been developed that are capable of studying paintings [11–13] and analyzing handwritings [14].

Figure 2.3 presents a case in which machine learning was used combined with hyperspectral imaging as a mitigation strategy. Machine learning methods can be subdivided into four types: supervised machine learning, unsupervised machine learning, semi-supervised learning, and reinforced machine learning [15–17]. Especially,

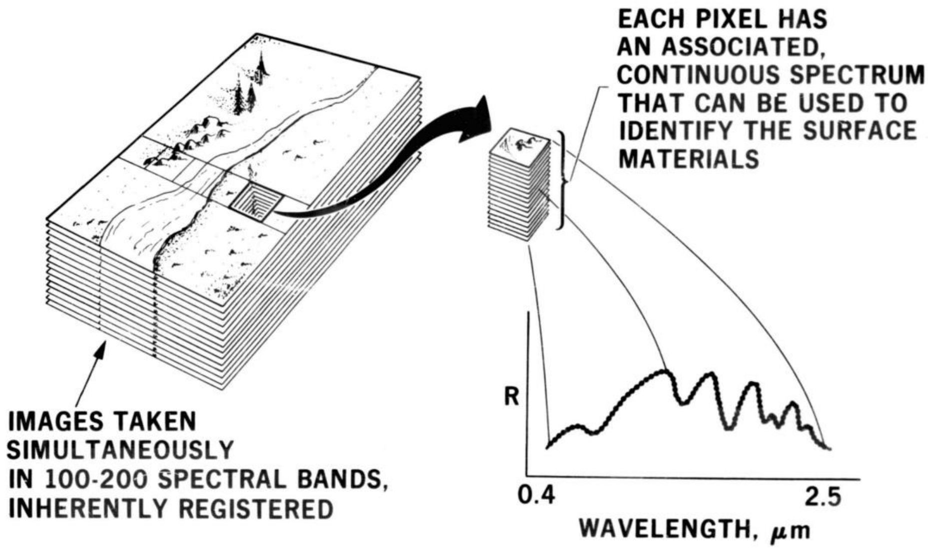

Figure 2.1 The concept of an imaging spectrometer obtaining a series of spectral images simultaneously and allowing a spectrum to be derived for each pixel [2].

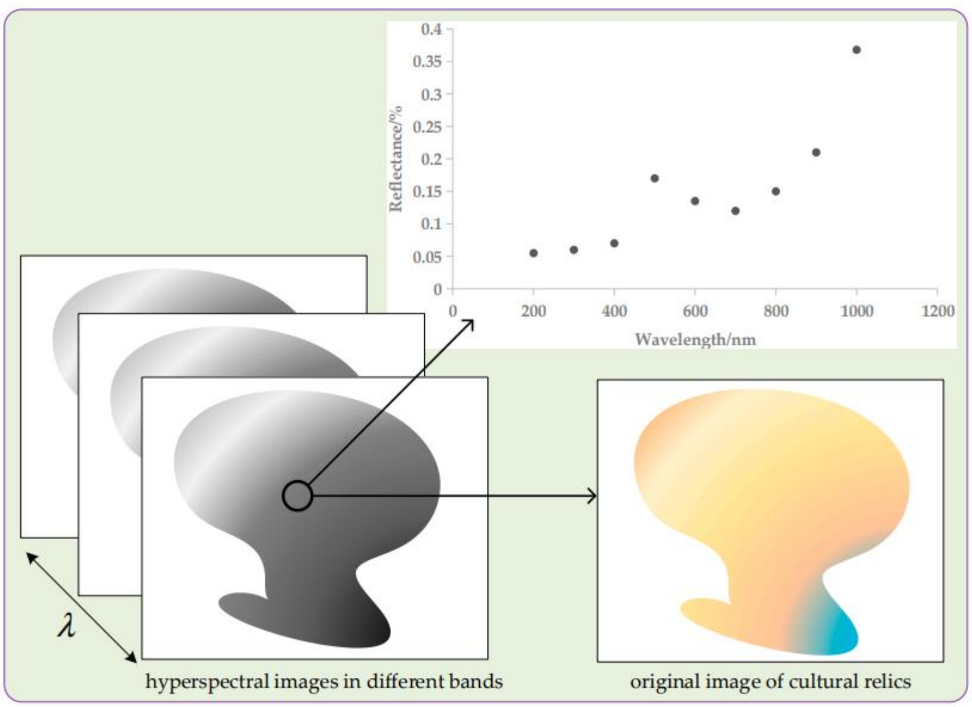

Figure 2.2 Schematic of the hyperspectral reflectance curve at a certain point [6].

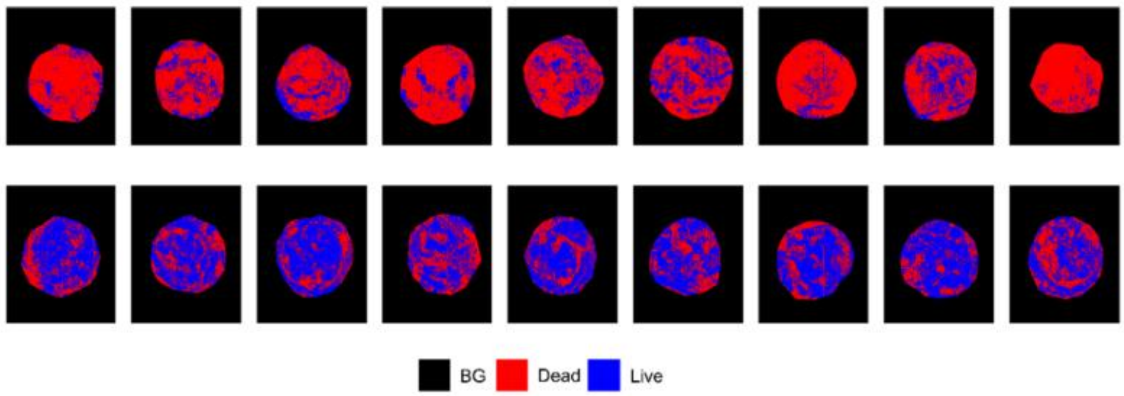

Figure 2.3 Classification of spores based on physiological state using results from CNN model [8].

supervised machine learning has two dominant methods that are classification and regression and algorithms such as support vector machine (SVM), random forest (RF), and convolutional neural networks (CNN) exist [18]. The study used a 1D-convolutional neural network (CNN) and random forest (RF) to detect and quantify spores in a complex food matrix of a mashed potato [8]. The acquired data is shown in Figure 2.3 and the related study also distinguished the live and dead spores with an overall accuracy of 90–94% when the dead/inactivated spores were present and absent. The use of machine learning and chemometrics improved the detection efficiency and decreased the background noise and made hyperspectral imaging a reliable detection method.

Figure 2.4 shows an illustration of hyperspectral imaging analysis of bloodstained marks. Blood is a fluid connective tissue that is composed of a mixture of cells, enzymes, and proteins and is frequently found in a crime scene [19]. Bloodstain identification methods have been developed so that crime scene examiners can perform subsequent analyses and have a better understanding of the circumstances surrounding a violent crime [20]. When it comes to fingerprints that are contaminated with blood, preserving the ridge details of the fingerprints in a crime scene is significant for identification purposes. Work was developed to prove that hyperspectral imaging can be used to distinguish common red/brown contaminants from bloodstained fingerprints and is capable of visualizing the ridge details [21,22]. Also, research was done on bloodstain detection on colored substrates [23,24].

Figure 2.5 and Figure 2.6 are examples of hyperspectral imaging used in cerebral surgery. The purpose of brain cancer surgery is the resection of the tumor and processing hyperspectral images using a deep learning-based framework has been a trend that made it possible to acquire accurate results [25,26]. Since hyperspectral imaging systems are advantageous in presenting the composition of spatial and spectral information, it has been widely used to provide diagnostic information about the physiological, morphological, and biochemical components of tissues and organs. Especially in brain imaging studies and cerebral disease research, hyperspectral imaging is considered a powerful tool. Hyperspectral imaging has been used to monitor brain oxygenation, hemodynamics [27–30] and diagnose brain cancer [31,32].

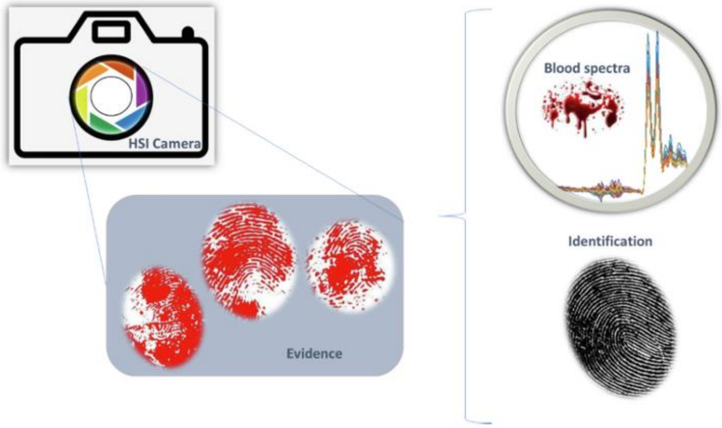

Figure 2.4 Illustrative schematic of hyperspectral imaging analysis of bloodstained marks [9].

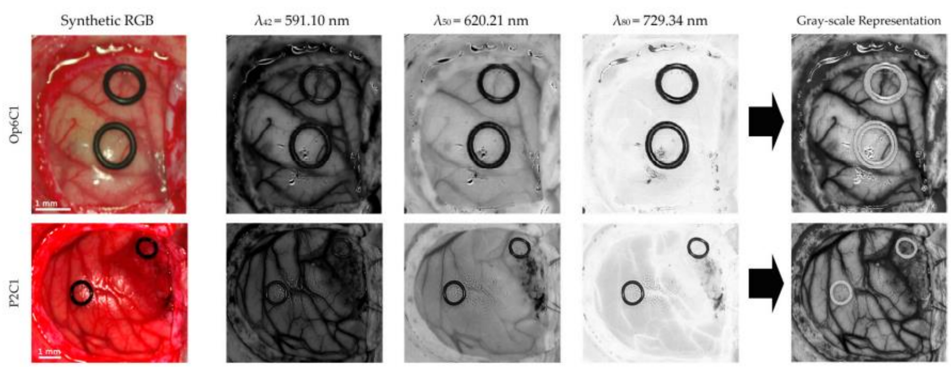

Figure 2.5 Gray-scale representation image examples and the corresponding three selected spectral channels employed in the three-band combination for the parenchymal and blood vessel detection. A synthetic RGB image is also included for comparison [25].

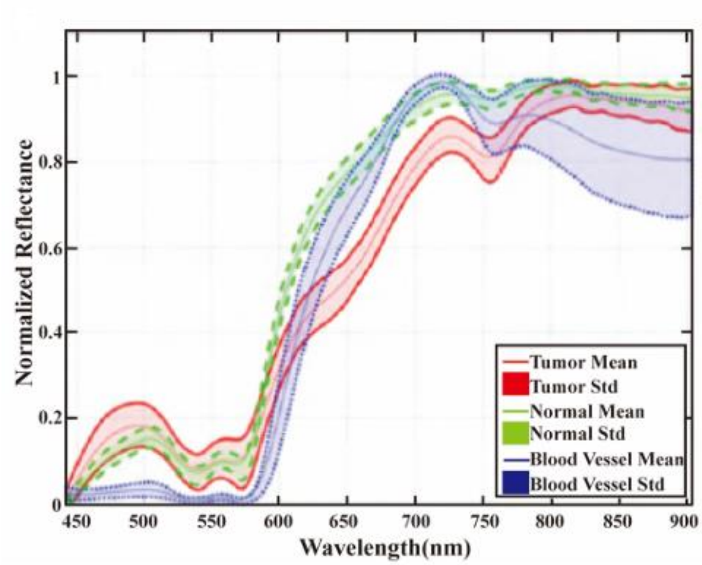

Figure 2.6 Spectral feature information of several brain tumor tissues in the visible-near infrared (VNIR) range at the pixel of regions of interest [10].

2.2 Hyperspectral Imaging for Temperature and Emissivity Measurements

In recent works by Devesse et al. [33,34] the visual method and hyperspectral method were used to collect the geometric information and the temperature and emissivity of the melt pool, respectively. The Laser Metal Deposition (LMD) technique deposits material in a melt pool that is created by a high-power laser beam. In additive manufacturing, it is essential to have a system that can monitor the real-time process to improve the quality of the printed material. This work presented a new measurement system that is capable of measuring the temperature and emissivity of the melt pool without being in contact with it. The fiber laser that was used to create the melt pool had a wavelength of 1,064 nm, a focus spot diameter of 1,000 μm, and a flat-top beam profile. The laser heated the surface of a substrate of AISI 316L stainless steel that was 20 mm thick by varying the laser power to 280 W, 320 W, 360 W, and 400 W. The metal powder was injected into the melt pool at a mass flow rate of 3 g/min. The monochrome visual camera was coaxially positioned with the laser and the hyperspectral line camera was inclined at an angle of 38 degrees relative to the surface normal. Figure 2.7 and Figure 2.8 show the side and top view of the measurement setup for the transverse and longitudinal measurements, respectively.

The spectral radiance B ($W \cdot sr^{-1} \cdot m^{-3}$) that is emitted by a blackbody was derived from Planck's law as a function of the wavelength λ and temperature T. Additionally, the emitted spectral radiance E_i of a real body measured at λ_i (i = 1,…, N_λ) wavelength was calculated by modifying the blackbody equation B by the spectral emissivity parameter ε_λ and including the measurement noise n_i. This relationship is described by Equation (2.1).

$$E_i = \varepsilon_\lambda(\lambda_i) B(\lambda_i, T) + n_i \tag{2.1}$$

The spectral emissivity ε_λ for metals was expressed as a linearly decreasing function of wavelengths in the visible and near-infrared (VNIR) range. This relationship is described by Equation (2.2).

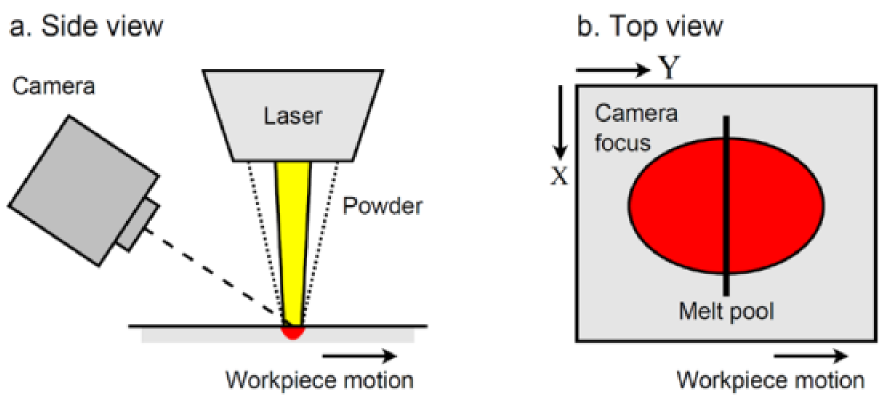

Figure 2.7 Side view (a) and top view (b) of transverse laser cladding [34].

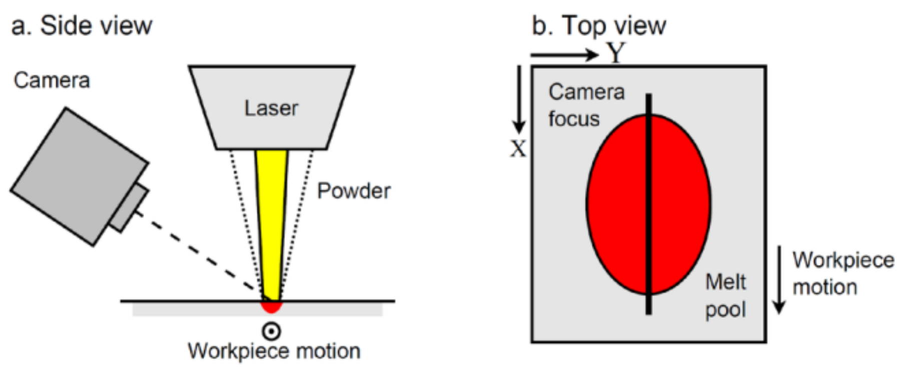

Figure 2.8 Side view (a) and top view (b) of longitudinal laser cladding [34].

$$\varepsilon_\lambda(\lambda) = B_\varepsilon - A_\varepsilon \frac{\lambda - \lambda_1}{\lambda_{N_\lambda} - \lambda_1} \tag{2.2}$$

where the constants A_ε and B_ε are restricted by $0 \leq A_\varepsilon < B_\varepsilon \leq 1$ to have a negative slope.

Assuming that the mean noise n_i is zero and the Gaussian variance is known as ${\sigma_{E_i}}^2$, the measured spectrum $E_i(\lambda_i, T)$ was fitted to a blackbody model $B(\lambda_i, T)$ with a linearly decreasing spectral emissivity ε_λ and it became a least squares problem. This relationship is shown in Equation (2.3).

$$(A_\varepsilon, B_\varepsilon, T) = argmin \sum_{i=1}^{N_\lambda} \frac{\left| E_i - \left(B_\varepsilon - A_\varepsilon \frac{\lambda_i - \lambda_1}{\lambda_{N_\lambda} - \lambda_1} \right) B(\lambda_i, T) \right|^2}{{\sigma_{E_i}}^2} \tag{2.3}$$

The solution is obtained by either setting slope A_ε to zero, using graybody assumption, or setting the B_ε offset to 1. As a result, the upper and lower bounds of the melt pool temperature and emissivity were calculated. The image binarization was done using different threshold levels that were multiples of Otsu's threshold [35]. The melt pool was divided into three regions (liquid, mushy, and solid) and the average temperature and average emissivity were derived. Figure 2.9 and Figure 2.10 show the transverse and longitudinal temperatures and emissivity profiles when the laser power is 320 W. In the figures, the red and blue curves correspond to the upper and lower temperature bounds and the dashed vertical lines indicate the melt pool width for Figure 2.9 and length for Figure 2.10. Depending on the different binarization levels (Otsu's threshold), the calculated melt pool width and length varied, and the results are displayed in Table 2.1 and Table 2.2, respectively. Surely, the power of the laser had an impact on the melt pool width and length.

The most recent work on thermal imaging of a melt pool developed an experimental method to image the melt pool temperature with a single commercial color camera and compared the results with multi-physics computational fluid dynamic (CFD) models [36]. The advantage of this approach was that since it leverages the principle of two-color thermal imaging, the temperature was easily imaged without the knowledge of the melt

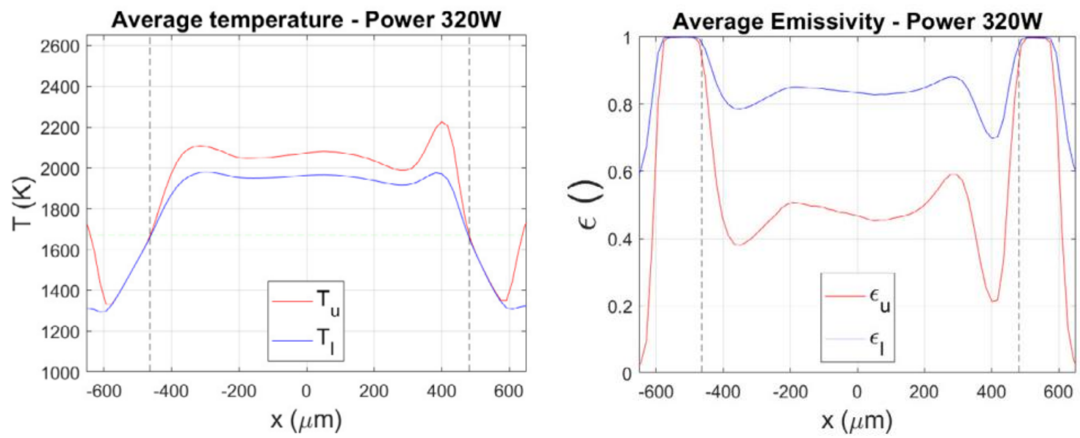

Figure 2.9 Transverse temperature and emissivity profile at 320 W laser power [34].

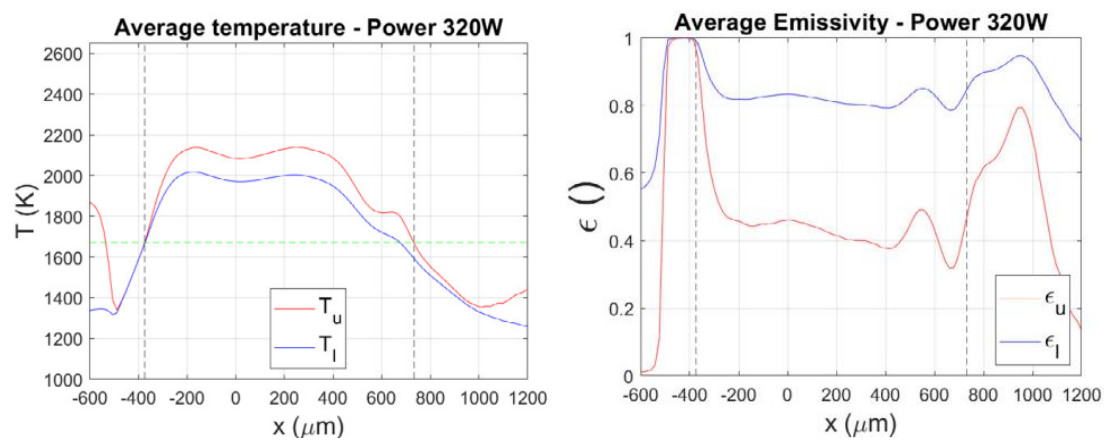

Figure 2.10 Longitudinal temperature and emissivity profile at 320 W laser power [34].

Table 2.1 Comparison of the calculated width between the hyperspectral and the visual method [34].

Power (W)	Hyperspectral Width (μm)	Visual Width for Threshold 1 (μm)	Visual Width for Threshold 0.5 (μm)
280	901.97	933.2	1023
320	945.11	941.5	1038
360	958.11	945.5	1038
400	972.27	968.18	1054

Table 2.2 Comparison of the calculated length between the hyperspectral and the visual method [34].

Power (W)	Hyperspectral Length (μm)	Visual Length for Threshold 0.5 (μm)	Visual Length for Threshold 0.25 (μm)
280	944.37	1110	1221
320	1106.79	1153	1277
360	1228.35	1201	1360
400	1334.34	1188	1396

pool emissivity, plume transmissivity, and the camera's view factor.

In the work of Gorevoy [37], it was proved that locating the spectral bands equidistantly is not good enough to minimize the error of temperature measurement. Instead, a better approach is to derive specific wavelengths and position the two narrow spectral bands near the derived wavelengths since the spectral bands define the temperature measurement precision. Snapshot hyperspectral imaging systems are highly recommended for thermography since they offer adjustable numbers, locations, and orders of selected spectral bands. This enables multiple collection modes, optimized data volume, and processing time. The principle of imaging spectroscopy is shown in Figure 2.11. A data cube $I(x, y, \lambda)$ is acquired and the temperature distribution T(x,y) is calculated by analyzing the spectrum $I(\lambda)$ in each pixel(x,y).

Figure 2.12 shows the flow chart of the overall process deciding the optimal wavelengths and minimizing the measurement errors. It was previously proved that the optimal wavelengths λ_1 and λ_2 are found by minimizing var [T]. The result is valid for different mean[n_k] values, but the integration times t_k should be the same. Equation (2.4) and Equation (2.5) show how var [T] and t_k is calculated.

$$var[T] = \frac{T^4}{C^2{}_2 t_s} \frac{2((s(\lambda_1))^{-1} + ((s(\lambda_2))^{-1}}{(G_1 - G_2)^2} \tag{2.4}$$

$$t_S = \frac{nK}{2} \; ((s(\lambda_1))^{-1} + ((s(\lambda_2))^{-1} \tag{2.5}$$

where G_k is expressed in Equation (2.6).

$$G_k = \lambda_k{}^{-1} \frac{\exp\,(C_2 T^{-1} \lambda_k{}^{-1})}{\exp\left(C_2 T^{-1} \lambda_k{}^{-1}\right) - 1} \tag{2.6}$$

Also, the correlation coefficient between ε and T is shown in Equation (2.7).

$$corr[\varepsilon, T] = -\frac{G_1 + G_2}{\sqrt{2(}G^2{}_1 + G^2{}_2)} \tag{2.7}$$

The existence of the optimal wavelengths that minimize the variance of temperature was proved by the above equations.

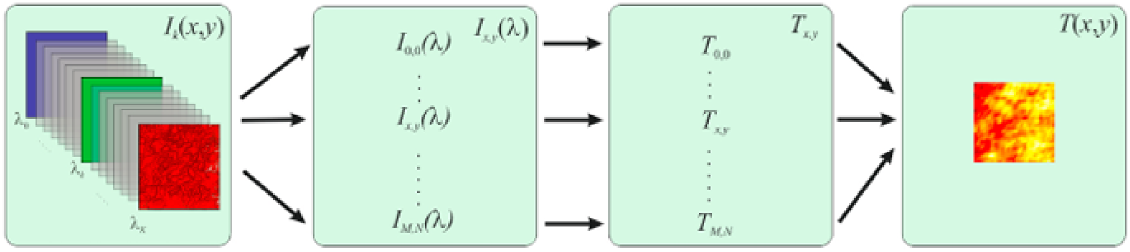

Figure 2.11 Imaging spectroscopy approach to temperature mapping [37].

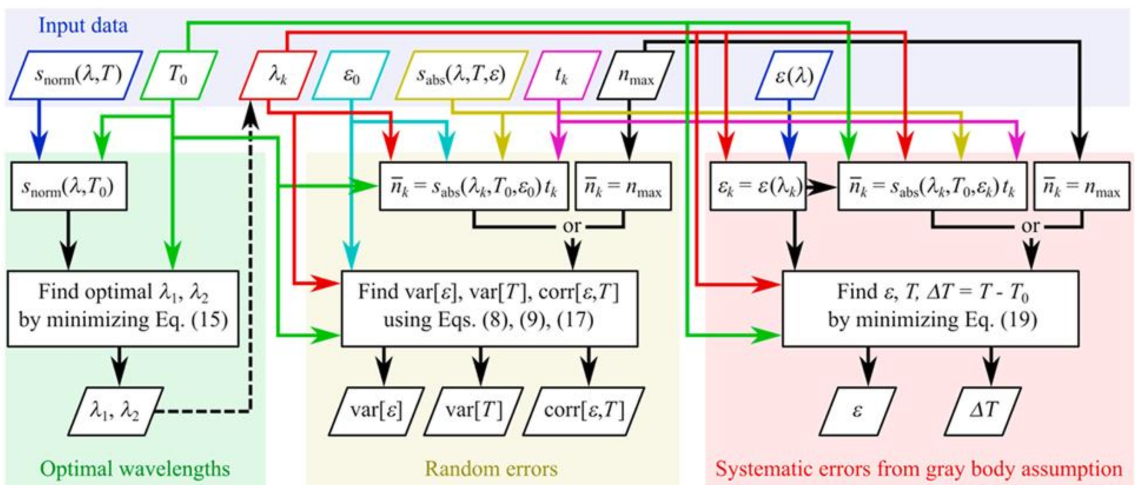

Figure 2.12 Flowchart of calculating optimal wavelengths and measurement errors [37].

function was written as Equation (2.8).

$$p = argmin_{\varepsilon,T} \sum_{k=1}^{K} \overline{n_k} \left(1 - \frac{\varepsilon}{\varepsilon_k} \frac{\exp\left(C_2 {T_0}^{-1} {\lambda_k}^{-1}\right) - 1}{\exp\left(C_2 T^{-1} {\lambda_k}^{-1}\right) - 1}\right)^2 \tag{2.8}$$

This allowed finding the systematic error of the estimated temperature as $\Delta T = T - T_0$. To summarize, once the sample temperature T_0 and the normalized spectral function $S_{norm}(\lambda_k, T)$ is known, the two optimal wavelengths for temperature measurement of a graybody sample with unknown emissivity were readily found.

An experiment was performed to apply the theory. Figure 2.13 shows the experimental setup and Figure 2.14 shows the diagram of the setup. Before the experiments, calibration was performed by calculating the spectral and intensity correction coefficients. The achromatic doublet L1 (f = 400 mm) images the specimen S, collimates the beam, and makes it focused on the pupil of the acousto-optical tunable filter (AOTF). The AOTF consists of three polarizers (P1, P2, and P3) and two wide-aperture non-collinear acousto-optical (AO) cells (AOC1 and AOC2). The light is in Bragg condition and the light changes the orientation of the polarization by diffracting on the volume grating in AOC1. The radiation that is not diffracted passes through AOC 1 but is filtered by P2 and this is done similarly by AOC2 and P3. After spectral filtration, the L2 lens which is identical to L1 focuses the light on the monochrome camera CAM. By using the high-frequency generator HFG and high-frequency amplifier HFA, the ultrasound frequency f was varied, and the period of the diffraction grating in the AOCs was set to choose a particular wavelength. The overall data cube $I(x, y, \lambda)$ was obtained by sequentially setting the AOTF at different wavelengths λ_k and acquiring the spectral images. The experimental data acquired from the setup varying the current to 15 A and 20 A is shown in Table 2.3 and Table 2.4. The tables include the following parameters: amount K of the wavelengths, spectral range $[\lambda_{min}, \lambda_{max}]$, step $\Delta\lambda$, calculated mean and standard deviation values of temperature mean $[T]$, std $[T]$ and emissivity mean $[\varepsilon]$, std $[\varepsilon]$ and correlation coefficient corr [ε,T]. Also, the dependence of std $[T]$ on K for the equidistant and optimized location of wavelengths for 15 A and 20 A is shown in Figure 2.15. Figure 2.16 shows the theoretical and experimental results by demonstrating the relationship of

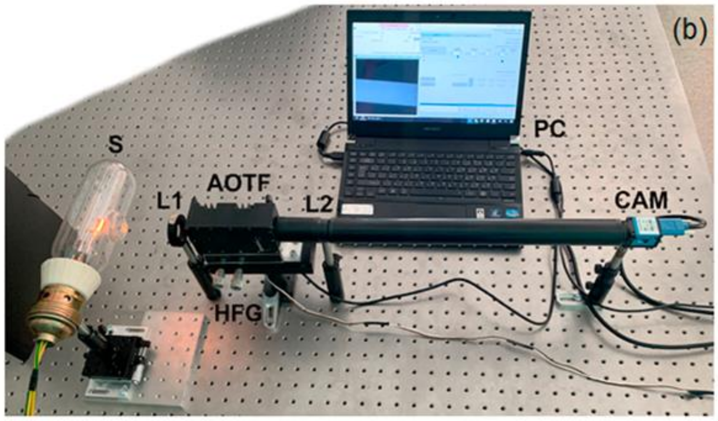

Figure 2.13 Experimental setup [37].

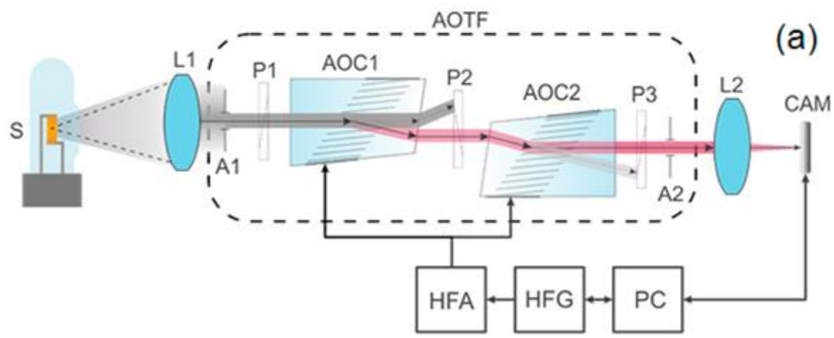

Figure 2.14 Diagram of the setup [37].

Table 2.3 Experimental data (current of 15 A, integration time 0.5 s at each wavelength) [37].

λ_{min}:$\Delta\lambda$:λ_{max}, nm	K	mean[ε]	std[ε]	mean[T], K	std[T], K	corr[ε,T]
590:5:950	73	0.261	0.0053	1836	3.65	−0.989
590:10:950	37	0.258	0.0065	1837	4.47	−0.991
590:20:950	19	0.250	0.0079	1843	5.74	−0.992
590:40:950	10	0.244	0.0105	1848	7.88	−0.993
610:5:630, 870:5:890	10	0.226	0.0072	1862	6.07	−0.986
630:5:650, 870:5:890	10	0.259	0.0085	1834	6.19	−0.987

Table 2.4 Experimental data (current of 20 A, integration time 0.08 s at each wavelength) [37].

λ_{min}:$\Delta\lambda$:λ_{max}, nm	K	mean[ε]	std[ε]	mean[T], K	std[T], K	corr[ε,T]
590:5:950	73	0.320	0.0064	2200	5.01	−0.989
590:10:950	37	0.316	0.0076	2203	6.07	−0.991
590:20:950	19	0.295	0.0089	2220	7.75	−0.992
590:40:950	10	0.280	0.0115	2236	10.8	−0.993
610:5:630, 870:5:890	10	0.279	0.0079	2241	7.49	−0.984
630:5:650, 870:5:890	10	0.309	0.0094	2210	7.94	−0.986

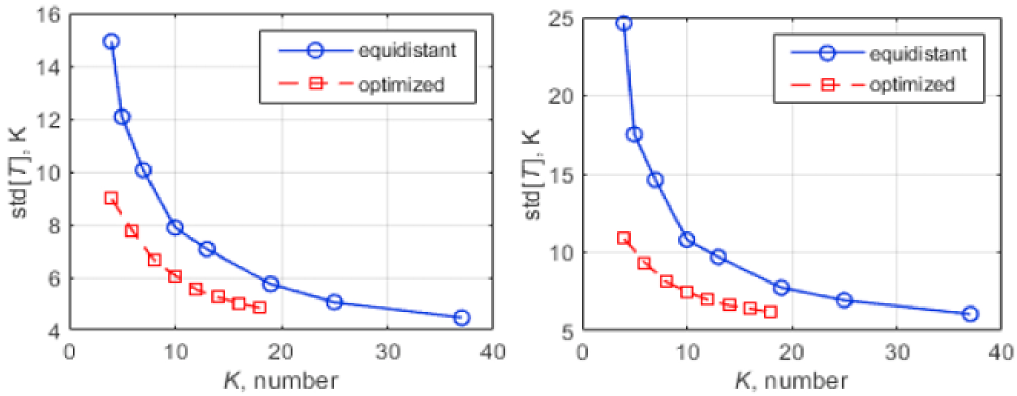

Figure 2.15 Experimental dependence of std $[T]$ on number K of wavelengths at current 15 A (left) and 20 A (right) [37].

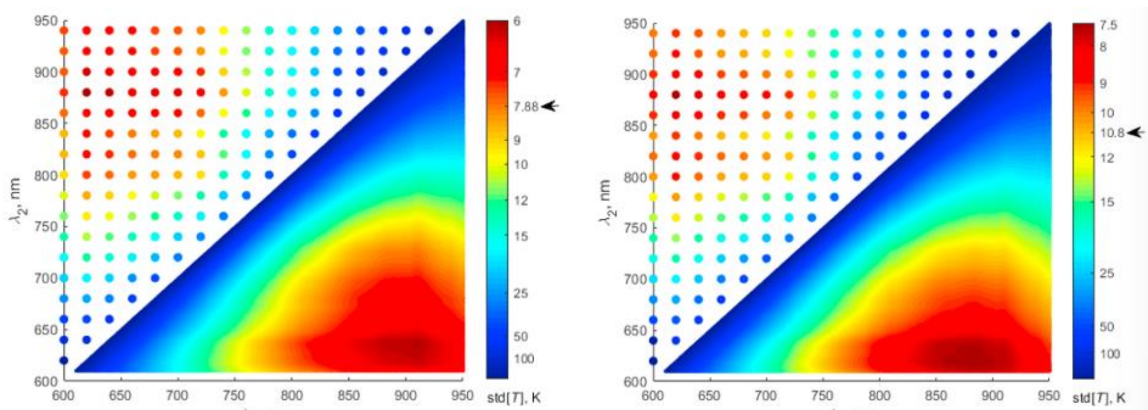

Figure 2.16 Experimental (upper triangle) and theoretical (lower triangle) distribution of std $[T]$ at a current of 15 A (left) and 20 A (right) [37].

std $[T]$ (standard deviation of measured temperature values) on the location of two wavelengths that were used for image acquisition (λ_1 and λ_2). The experimental data (upper triangle) was acquired for each pair λ_1 and λ_2 using 10 bands chosen as $(\lambda_1 - 10)nm{:}\,5{:}\,(\lambda_1 + 10)nm$ and $(\lambda_2 - 10)nm{:}\,5{:}\,(\lambda_2 + 10)nm$. The theoretical data (lower triangle) was derived in accordance with Equation (2.4) by applying $S(\lambda)$. Afterward, the data was normalized to make both minimum values equal. The black arrow in Figure 2.16 indicates the values of the equidistant location of 10 bands. From this work, it has been proved that the data volume and processing time of a hyperspectral technique that measures temperature and emissivity can be optimized. Also, a new method was proposed that derives specific wavelengths and locates the two narrow spectral bands near the derived wavelengths. This method turned out to be more successful than the conventional method that positions the spectral bands equidistantly. For the presented algorithm, the optimal spectral bands should be chosen based on the range of the temperature being measured and the spectral characteristics of the system. Moreover, research determining temperature using long-range thermal emission spectroscopy [38] and analyzing the impact of the temperature on the spectral shift in ultraviolet hyperspectral imaging spectrometers was done [39].

2.3 Compressed Single-shot Hyperspectral Imaging

Research was conducted using hyperspectral imaging for combustion diagnostics [40]. The purpose of the paper was to measure the ${C_2}^*$ and CH^* chemiluminescence emissions of a methane/air flame at various equivalence ratios by applying the compressed hyperspectral imaging technique. A block diagram of the compressed hyperspectral imaging technique is shown in Figure 2.17. The compressed hyperspectral imaging technique is performed by acquiring the emitted or reflected light from an object and modulating the light with a random binary pattern that has sparsity. A digital micromirror device (DMD) was used to encode the light in this experiment and the modulated light was collected by a spectrometer. The acquired hyperspectral image consists of two spatial axes (x and y) and a spectral axis (λ) and the information is gathered and processed by a

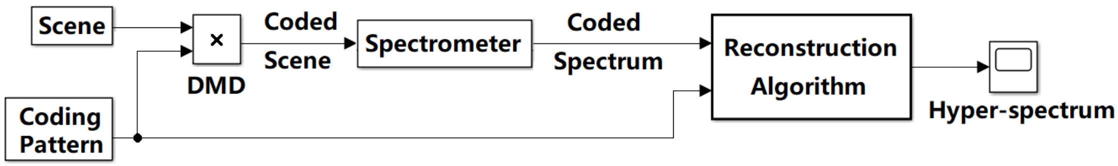

Figure 2.17 Block diagram of compressed hyperspectral imaging technique [40].

reconstruction algorithm. The compressed hyperspectral augmented image reconstruction (CHAIR) algorithm is based on the two-step iterative shrinkage/thresholding (TwIST) algorithm [41]. Figure 2.18 shows an illustration of the CHAIR algorithm. The algorithm uses a bilateral filter to improve the recovered image quality and generates a 3D cube that contains the 2D image and the 1D spectral data. Each cube slice corresponds to a specific wavelength and is incrementally shifted away from the other slices along the wavelength axis. The TwIST algorithm is utilized afterward to reconstruct the hyperspectral image. The algorithm scans the hyperspectral slices using the image of the modulation pattern and gets rid of the residuals of the coding pattern. A bilateral filter is used to eliminate white noise from the reconstructed hyperspectral slices, and it was proved that the nonuniform intensity distribution of the encoded signal can be corrected by the TwIST algorithm. The experimental setup is shown in Figure 2.19. The non-premixed methane/air flat flame emissions of CH^* (430 nm) and ${C_2}^*$ (515 nm) from a Hencken burner was imaged using optics, a pair of camera lenses, a DMD, a spectrometer, and a PI-MAX4 ICCD camera. The light from the flame was collected by optics, went through the camera lens, and arrived at the DMD. The DMD used in the experiment had 1,120 $\times$ 912 micromirrors and was mounted on a microelectromechanical system (MEMS) so that it can respectively rotate 12 degrees in both directions. A sparse random pattern was displayed on the DMD, and the DMD modulated the light reflected from the flame by adjusting the position of the micromirrors. The spectrometer slit was fully opened to preserve the spatial data of the spectrum. The flame temperature ranged from 1,992 K to 2,092 K and it depended on the equivalence ratio (0.8 to 1.25) of the inbound gas. Figure 2.20 and Figure 2.21 show the acquired data from the experiment. Figure 2.22 shows the linear relationship between the ratio of CH^* and ${C_2}^*$ emission intensities and the corresponding equivalence ratios. The error range was $\pm$0.224 % and $\pm$0.535 % for the recovered data and ground truth data, respectively.

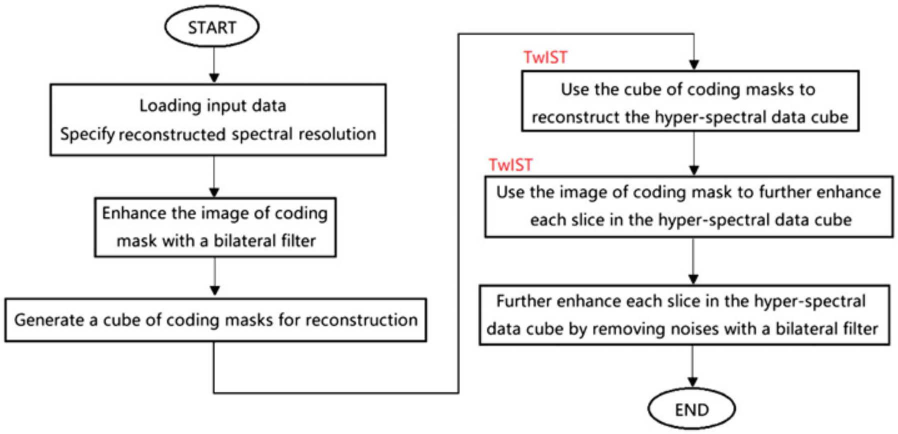

Figure 2.18 Compressed hyperspectral augmented image reconstruction (CHAIR) algorithm [40].

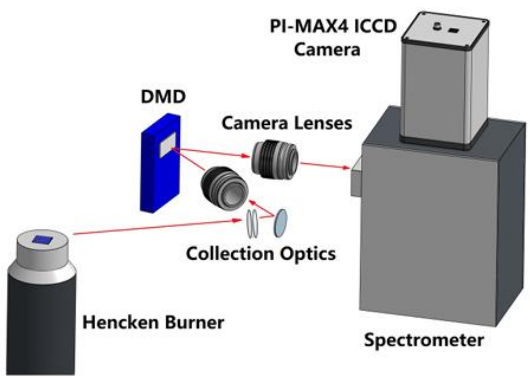

Figure 2.19 Diagram of the experimental setup [40].

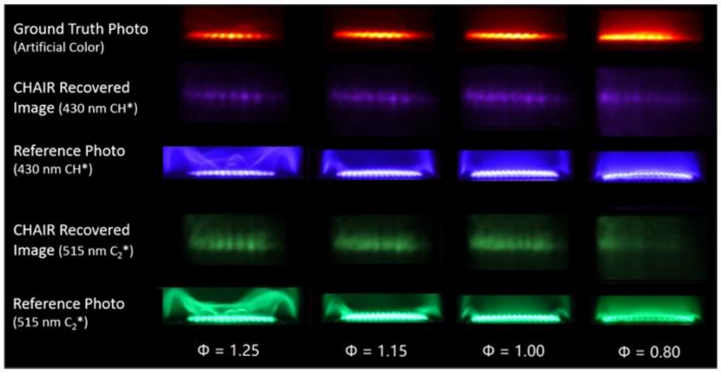

Figure 2.20 Comparison between acquired data [40].

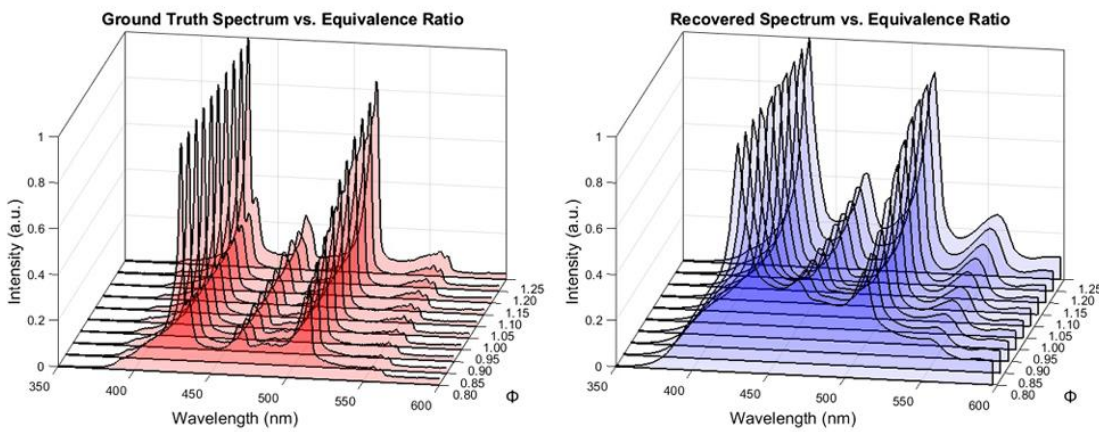

Figure 2.21 The recovered spectral data [40].

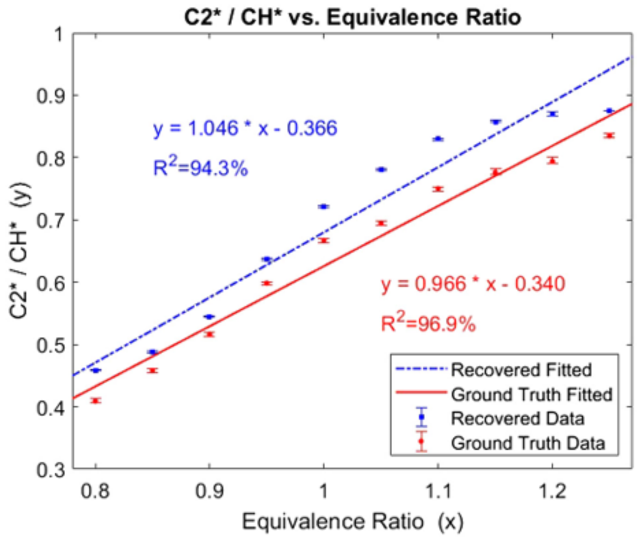

Figure 2.22 The linear relationship between the ratio of CH^* and ${C_2}^*$ emission intensities and the corresponding equivalence ratio. The error bars in the figure represent the minimum and maximum values measured at each data point [40].

CHAPTER THREE
EXPERIMENTAL METHODS AND TECHNIQUES

3.1 Overview

To acquire the optimized results in terms of the image and spectra resolution, three preliminary experiments were done to determine the modulation pattern, to investigate the impact of the spectrometer slit width on the recovered results, and to get the temperature calibration data (ground truth data) at a certain temperature (1,020 ℃). Afterward, the final experiment was conducted to perform the 2D temperature map acquisition.

3.2 Pattern Determination to Optimize the Image Quality of HSIS

The purpose of the experimental setup in this case was to determine the modulation pattern that can facilitate the image reconstruction. A diagram of the configuration is shown in Figure 3.1. The compact fluorescent lamp (CFL) illuminates the Airforce target card, and the target scene was collected by an achromatic lens of 100 mm focal length. The image of an Airforce target card is shown in Figure 3.2. The red rectangle in Figure 3.2 indicates the field of view when the spectrometer slit was fully opened. The field of view width and length were 0.2 inches and 0.5 inches, respectively. The modulation pattern was positioned between the two achromatic lenses of 100 mm focal length and the scene was imaged onto the slit. A binary pattern was printed on a transparent film to be used as a modulation pattern. Nine patterns were tested using the experimental setup based on how many pixels are there per inch (300 ppi, 700 ppi, and 1,000 ppi) and how much percentage of the dots covered the whole pattern area (20 %, 25 %, and 30%). One of the modulation patterns used for the experiment is shown in Figure 3.3. A spectrometer (SpectraPro HRS 300) and a PI-MAX electron-multiplying charge-coupled device (EMCCD) camera were used for the experiment. The center wavelength of the spectrometer was set to 0 nm and the exposure time of the EMCCD camera was set to 5 ms for imaging purposes.

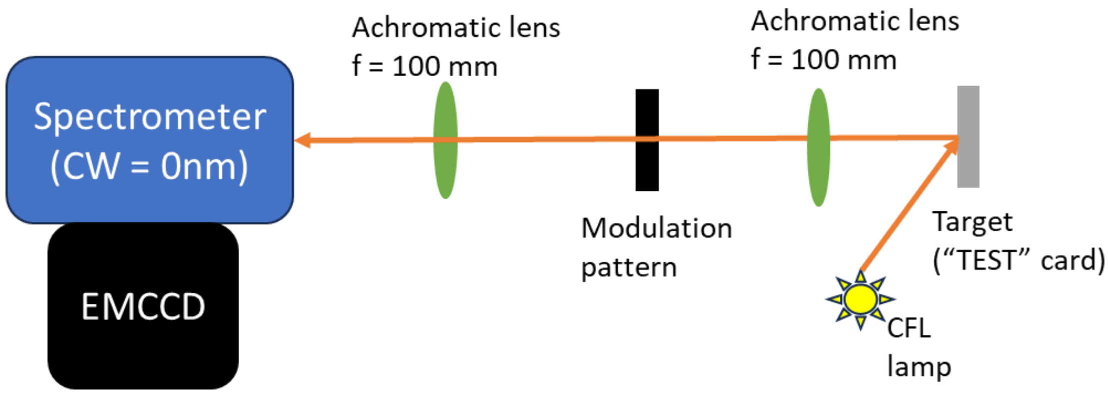

Figure 3.1 Diagram of the setup.

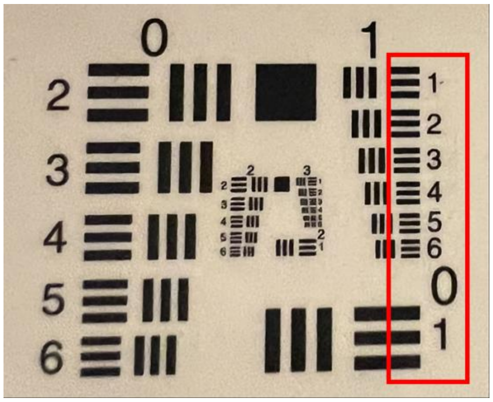

Figure 3.2 Airforce target card (the red rectangular region is the field of view of the setup width: 0.2 inches and length: 0.5 inches).

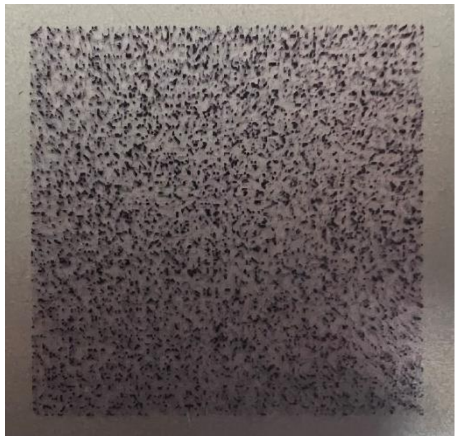

Figure 3.3 Binary modulation pattern (700 ppi, 20 % dot concentration).

3.3 Demonstration of the Concept of the CHAIR Algorithm

The purpose of this experiment was to demonstrate the concept of the CHAIR algorithm by varying the spectrometer slit size to four different values. In total, four slit widths were tested using the current experimental setup. The tested values were 3.02 mm (fully open), 1.52 mm (50 % open), 0.77mm (25% open), and 0.47 mm (15% open). The image reconstruction and the comparison of the true spectrum and the acquired spectra were done for each case. The experimental setup is shown in Figure 3.4. Prior to the experiment, a Neon Argon lamp was placed right in front of the slit for wavelength calibration for 580 nm. A green (λ = 532 nm) and red (λ = 632 nm) laser was used to illuminate the Airforce target card simultaneously and the modulation pattern (700 ppi, 20% dot concentration) was placed between the two achromatic lenses of 100 mm focal length. The captured scene was imaged onto the spectrometer slit. The spectrometer center wavelength and the spectrometer grating were selected to capture both spectral information in a single shot. For this experiment, the spectrometer center wavelength was set to 580 nm. Also, the spectrometer grating density was 300 g/nm and the spectrometer grating blaze was 500 nm. The wavelength coverage in this experimental setup was about 130 nm. The exposure time of the EMCCD camera was 60 ms and only one frame was acquired for four different slit widths.

3.4 Acquiring the Temperature Calibration Curve (Ground Truth Data) of 1,020°C

The goal of this experiment was to acquire a full spectrum of the graphite plate for a known temperature so that it could be used as ground truth data for HSIS. It should be noted that the ground truth data consists of two data sets: The data without the optical filter (continuous spectrum) and the data including the optical filter. The optical filter created three discrete points to facilitate the spectrum reconstruction process of the code. Diagrams of both experimental setups are shown in Figure 3.5 and Figure 3.6, respectively. Before the experiment, a Neon Argon lamp was placed right in front of the slit for wavelength calibration for 605 nm, 725 nm, and 845 nm. A 500W, 910 nm near-infrared range laser was used to heat the graphite plate. The size of the laser beam was 11 mm x 11 mm (square) and its focal length was 200 mm.

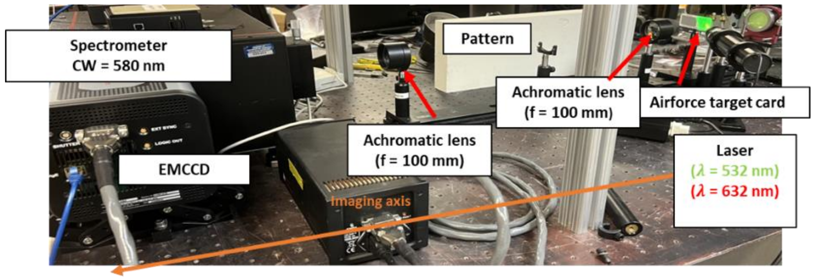

Figure 3.4 Experimental setup.

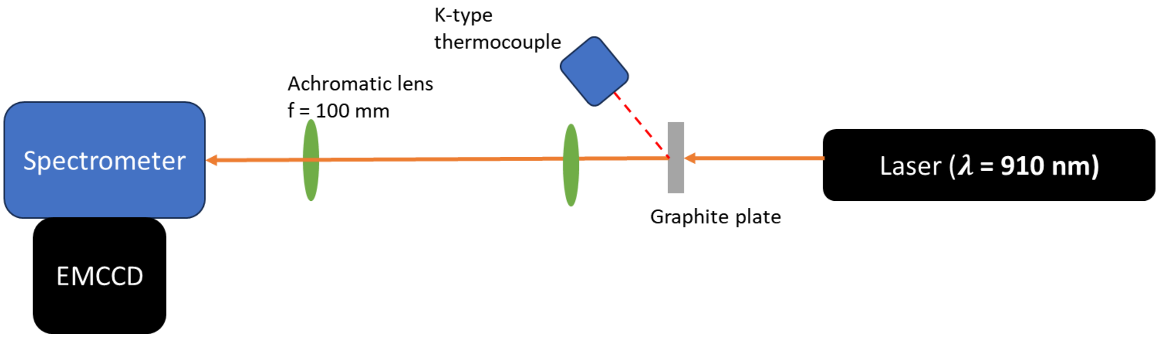

Figure 3.5 Experimental setup without the optical filter.

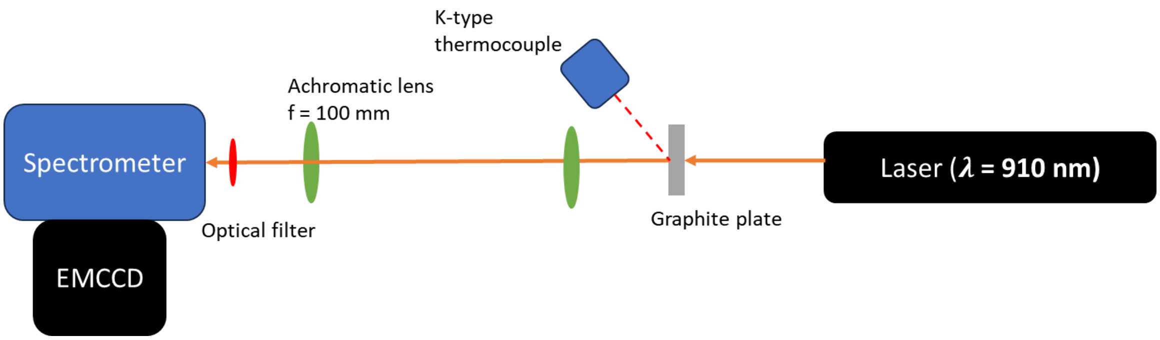

Figure 3.6 Experimental setup with the optical filter in position.

As the graphite plate (0.14 x 0.79 x 3.94 inches) was heated by the laser, a K-type thermocouple was used to measure the surface temperature of the opposite side of the graphite plate where it was heated. For this setup, the pattern was not in use, and the two achromatic lenses of 100 mm focal length were still present. All the captured spectral information was transmitted to the spectrometer and the EMCCD camera and was stored and processed as a spe file. To record the spectrum, the spectrometer slit size was 40 μm and the center wavelength of the spectrometer was set to 605 nm, 725 nm, and 845 nm based on the information that the current grating setting (grating density: 300 g/nm and grating blaze: 500 nm) is capable of recording around 130 nm for each shot. 50 images were recorded for each wavelength and the data was averaged for processing. The graphite plate was heated to 1,020 ℃ (1,293.15 K).

3.5 Acquiring a 2D Temperature Map Using HSIS at a 40μm Slit

Another experiment was done to recover the spatial and spectral data by using the HSIS. The experimental setup is shown in Figure 3.7. The goal was to reconstruct the spectral data based on the three peaks that were generated by the optical filter. Two center wavelengths 605 nm and 830 nm of the spectrometer were selected, and a Neon Argon lamp was placed right in front of the slit for wavelength calibration for 830 nm. The wavelength calibration for 605 nm was already done in the previous experiment. A 500W, 910 nm near-infrared range laser heated the graphite plate to 1,020 ℃ (1,293.15 K), and the K-type thermocouple was used to measure the surface temperature of the opposite side of the graphite plate where it was heated. The two achromatic lenses of 100 mm focal length were present, and the binary pattern was positioned between the lenses. All captured spectral information was transmitted to the spectrometer and the EMCCD camera by passing the optical filter in front of the spectrometer slit. Initially, the data was stored as a spe file and later extracted as a tiff file for data processing. To record the spectrum, the spectrometer slit size was 40 μm and the center wavelength of the spectrometer was set to 605 nm and 830 nm based on the information that the current grating setting (grating density: 300 g/nm and grating blaze: 500 nm) is capable of recording around 130 nm for each shot. 50 images were recorded for each wavelength

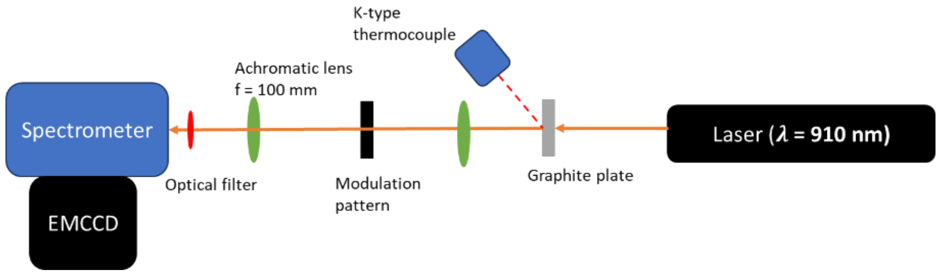

Figure 3.7 Experimental setup.

and the data was averaged for processing.

3.6 Acquiring a 2D temperature Map Using HSIS at a 3.02 mm Slit

An experiment was performed to acquire a 2D temperature map using HSIS. Figure 3.8 shows the experimental setup. A steel rod with an oxidized surface was positioned slightly in front of the graphite plate so that the HSIS could recover the image of a steel rod. A 500W, 910 nm near-infrared range laser heated the graphite plate to 1,020 ℃ (1,293.15 K), and the K-type thermocouple was used to measure the surface temperature of the opposite side of the graphite plate where it was heated. The modulation pattern (700 ppi, 20% dot concentration) was placed between the two achromatic lenses of 100 mm focal length. A neutral density (ND) filter (optical density 1.1 (1.0 + 0.1)) was used to reduce the intensity of the signal to make sure the acquired image was not oversaturated. Also, an optical filter (TB550/660/850) was used to facilitate the data processing by creating three peaks in the 543 – 558 nm, 653 – 668 nm, and 835 – 865 nm wavelength range. Two center wavelengths (605 nm and 830 nm) were used to collect the data at 1,020 ℃ with the slit 3.02 mm (3,020 μm) open. For the EMCCD camera, the exposure time was 5 ms and 50 frames were acquired for each center wavelength respectively.

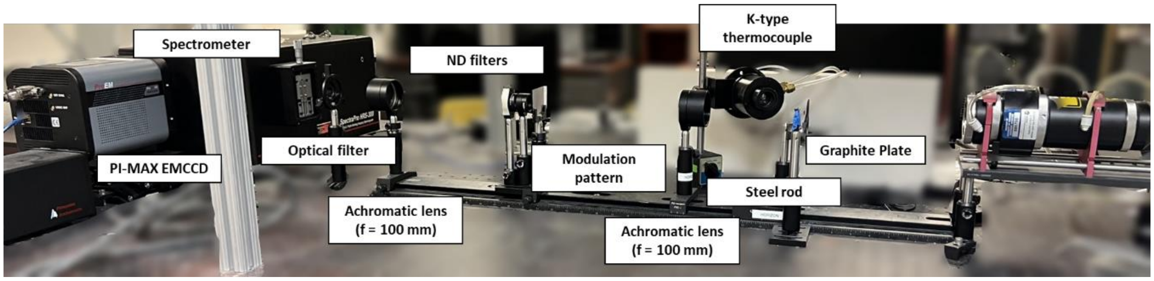

Figure 3.8 Experimental setup

CHAPTER FOUR
RESULTS AND DISCUSSION

4.1 Pattern Determination to Optimize the Image Quality of HSIS

Figure 4.1 shows the ground truth image, the modulated image, and the recovered image (recovery). The best pattern to yield a sharp reconstructed image was determined by comparing the line intensity profile of the recovered image to the ground truth image line intensity profile. The line pattern part of the Airforce target card was selected to get the line intensity profile. Figure 4.2 shows a red dotted line on the ground truth image, and this was the part selected to compare the ground truth image and the reconstructed image. The image was rotated 90 degrees counterclockwise and the 256^{th} to 455^{th} row and the 383^{rd} column were used for comparison. As a result, the pattern with 700 ppi and 20% dot concentration was chosen and used for the rest of the experiments. Figures 4.3 to 4.5 visualize the line intensity profile of the ground truth image and the reconstructed images using nine different patterns. Figure 4.6 shows the overall data comparing the best cases for each pixel-per-inch value. Also, Table 4.1 shows the calculated correlation coefficient values for each pixel-per-inch case. The 700 ppi and 20 % dot concentration pattern had a correlation coefficient value of 0.6715 and showed the strongest positive correlation with the ground truth image.

4.2 Demonstration of the Concept of the CHAIR Algorithm

Figures 4.7 to 4.10 show the reconstructed images and spectra for each case. All the recovered images proved that the algorithm was able to pick up the main features of the Airforce target card since the numbers and line patterns were identifiable in the reconstructed images. It was noticeable that as the spectrometer slit width decreases, the field of view of the image gets smaller. Additionally, the reconstructed spectral data showed that the 1D spectral reconstruction was successful and the quality of the reconstruction gets better as the spectrometer slit width decreases. This experiment was conducted to show that there is always a trade-off between the field of view of the image and the spectral data quality and it should be balanced to get the optimal results.

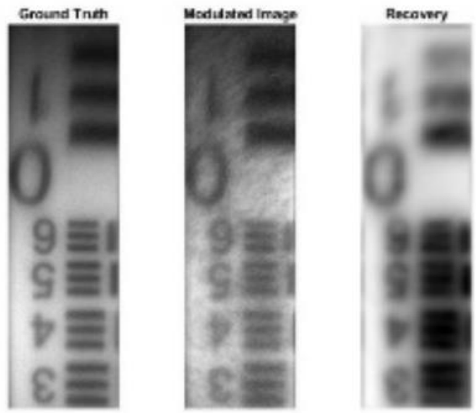

Figure 4.1 The ground truth image, modulated image, and recovered image.

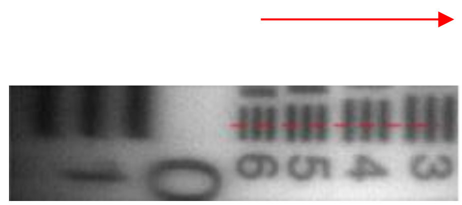

Figure 4.2 Line profile that was used to compare the ground truth image and the reconstructed image.

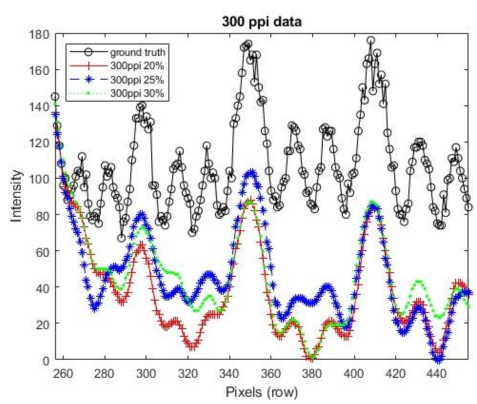

Figure 4.3 300 ppi results (line profile).

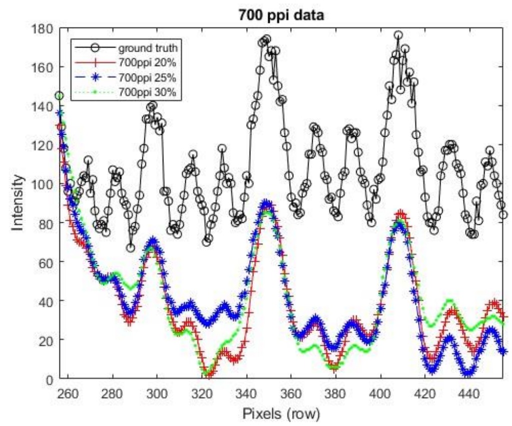

Figure 4.4 700 ppi results (line profile).

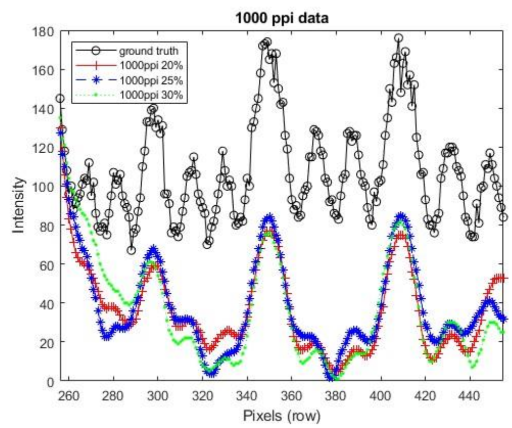

Figure 4.5 1,000 ppi results (line profile).

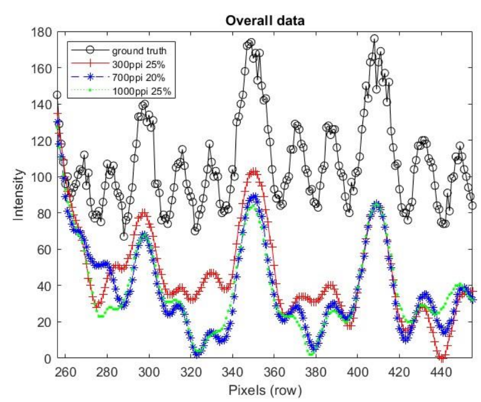

Figure 4.6 Overall data (line profile)

Table 4.1 Calculated correlation coefficients of ground truth intensity and recovered image intensity of each pattern.

	Correlation coefficient
300 ppi and 20 % dot concentration pattern	0.5865
300 ppi and 25 % dot concentration pattern	0.6617
300 ppi and 30 % dot concentration pattern	0.5247
700 ppi and 20 % dot concentration pattern	0.6715
700 ppi and 25 % dot concentration pattern	0.5787
700 ppi and 30 % dot concentration pattern	0.5227
1,000 ppi and 20 % dot concentration pattern	0.5981
1,000 ppi and 25 % dot concentration pattern	0.6491
1,000 ppi and 30 % dot concentration pattern	0.5113

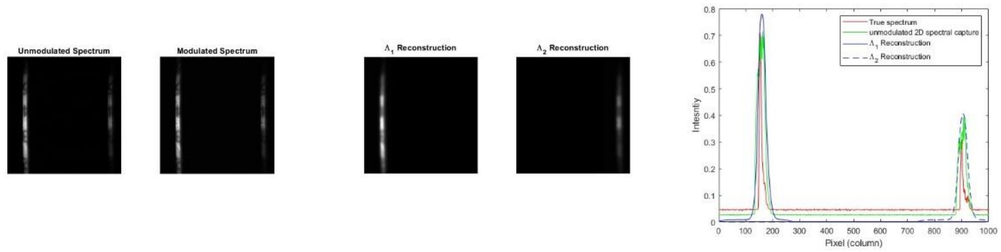

Figure 4.7 15% open slit width (0.47 mm) data. Unmodulated and modulated spectra (left), reconstructed spectra λ_1 (green laser) and λ_2 (red laser) (middle), and intensity profile of data (right).

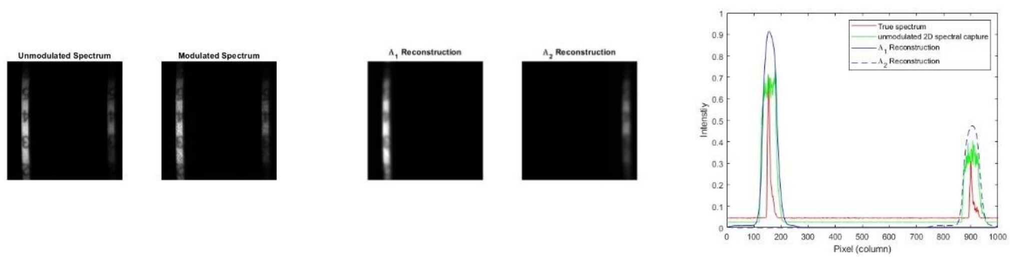

Figure 4.8 25% open slit width (0.77 mm) data. Unmodulated and modulated spectra (left), reconstructed spectra λ_1 (green laser) and λ_2 (red laser) (middle), and intensity profile of data (right).

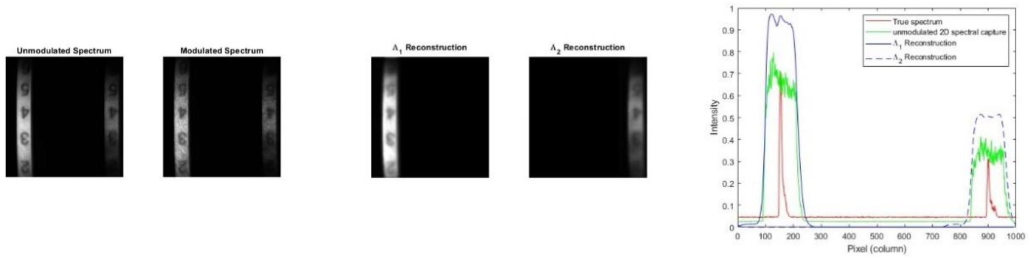

Figure 4.9 50% open slit width (1.52 mm) data. Unmodulated and modulated spectra (left), reconstructed spectra λ_1 (green laser) and λ_2 (red laser) (middle), and intensity profile of data (right).

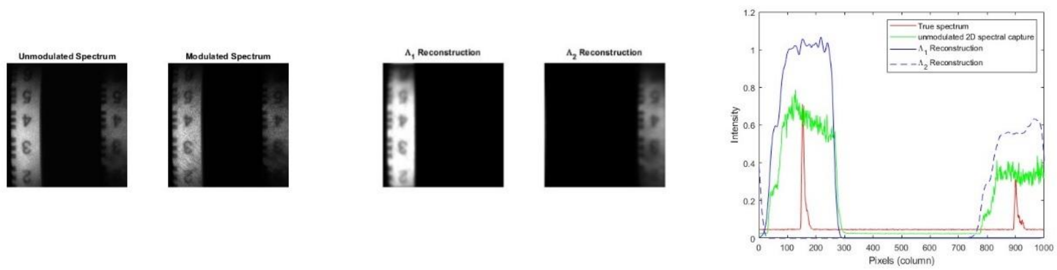

Figure 4.10 fully open slit width (3.02 mm) data. Unmodulated and modulated spectra (left), reconstructed spectra λ_1 (green laser) and λ_2 (red laser) (middle), and intensity profile of data (right).

Figures 4.7 to 4.10 show the unmodulated and modulated spectra, reconstructed spectra, and the intensity profile of the data. The 399th row was selected to get the intensity profile of the recovered spectrum. All the input images were normalized by their maximum intensity values before they were processed.

4.3 Acquiring the Temperature Calibration Curve (Ground Truth Data) of 1,020°C

Figure 4.11 shows the ground truth data without the optical filter and with the optical filter after being normalized by the continuous spectral ground truth data recorded without the optical filter. The optical filter (band-pass filter) gives passage only to the light in the selected wavelength ranges; 543 nm–558 nm, 653 nm–668 nm, and 835 nm–865 nm, and the tolerance is $\pm$ 10 nm. The acquired ground truth data had a range of 540–906 nm and the efficiencies of the spectrometer grating and the EMCCD camera were taken into account. Figure 4.12 shows the corrected ground truth data. The 1st and 2nd peak values were corrected to match the 1D continuous spectral data. The ground truth data with the optical filter will be used to evaluate the accuracy of the recovered spectrum for the subsequent experiments. Also, the emissivity was set to 0.95 based on the graybody assumption.

4.4 Acquiring a 2D Temperature Map Using HSIS at a 40μm Slit

Figure 4.13 shows the reconstructed image and Figure 4.14 shows the ground truth data with the optical filter and the reconstructed spectral data using the code. The three peaks were 561.349 nm, 665.678 nm, and 866.838 nm. The reconstruction algorithm uses the random pattern image as an input and recovers the data that has the same size as the random pattern image. Multiple slices of the data were used to reconstruct the spectral data. As the slit size increases, more spatial data can be acquired by a single shot, but the spectral data accuracy will decrease since the slit size has been increased. The reconstructed data shown in Figure 4.14 represent the maximum intensity value of the reconstructed image for each selected wavelength. The reconstructed data was normalized by the third peak value (same principle as the ground truth data with the optical filter). The camera quantum efficiency and the spectrometer grating efficiency

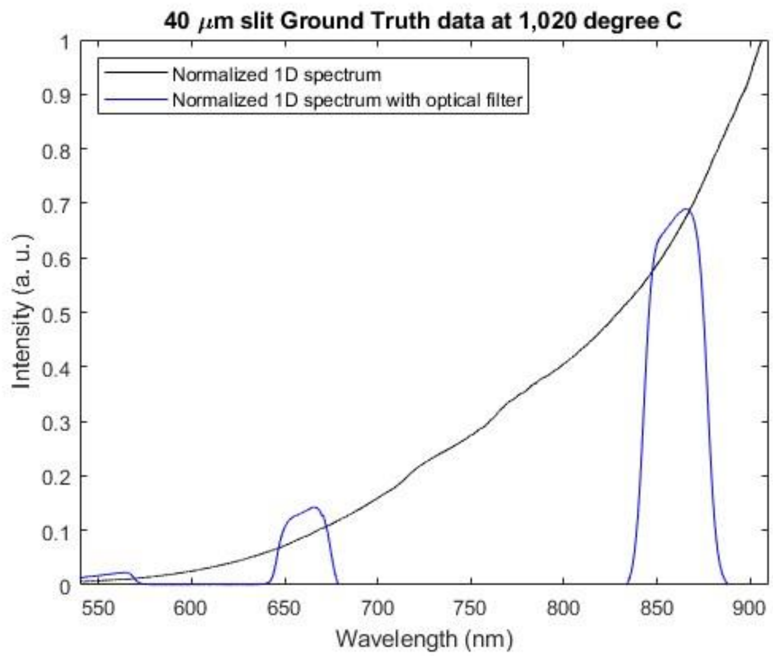

Figure 4.11 Ground truth data

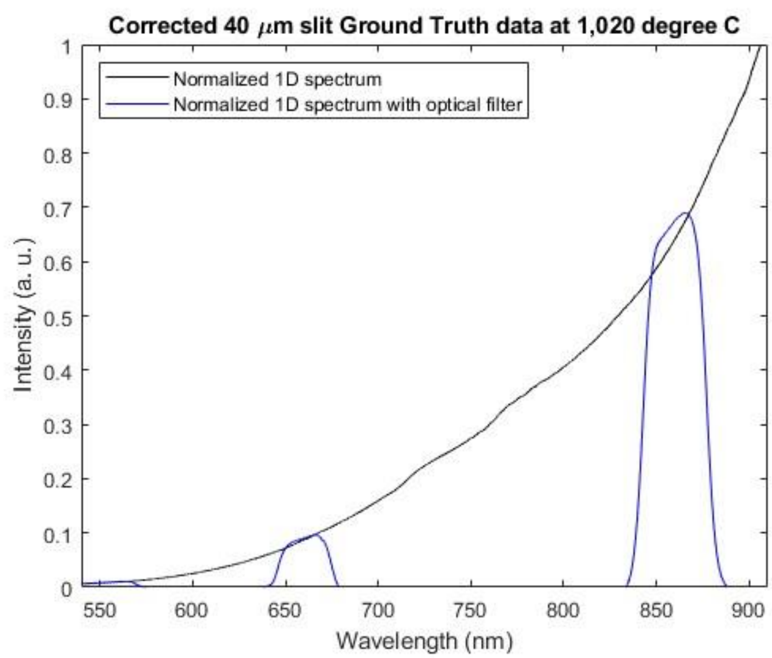

Figure 4.12 Corrected ground truth data

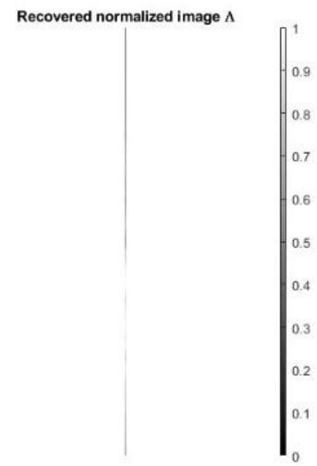

Figure 4.13 40 μm slit data image reconstruction result.

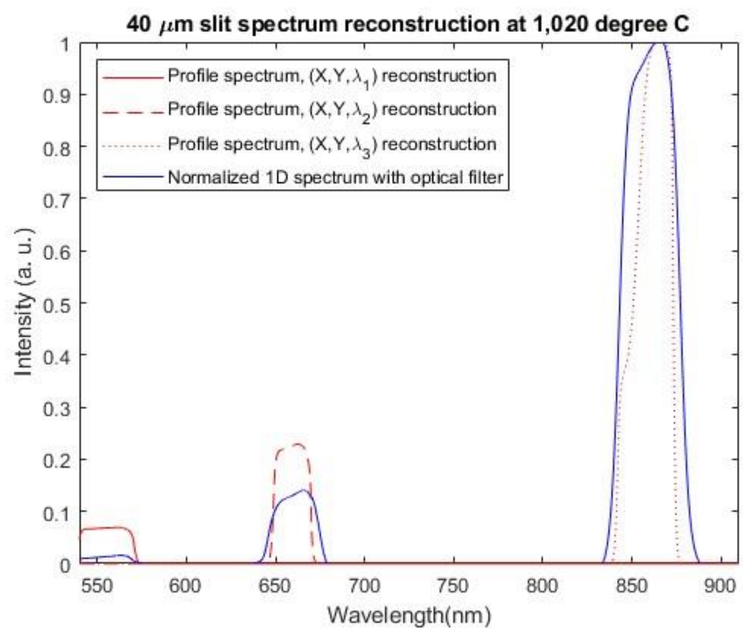

Figure 4.14 Reconstructed spectral data.

were considered during data processing.

The temperature calculation of the reconstructed spectrum was done by using the normalized second peak value. Here, the ratio (R) of the second peak value of the normalized recovered spectral data to the second peak value of the normalized ground truth data was calculated. Equation (4.1) shows the actual numerical value acquired from Figure 4.14.

$$R_{40\ \mu m\ slit} = \frac{Normalized\ recovered\ value_{\lambda_2}}{Normalized\ ground\ truth\ value_{\lambda_2}} = \frac{0.223264}{0.140518} \tag{4.1}$$

The experimental spectral radiance value that will be an input of a function to calculate the temperature was derived by multiplying the ratio (R) by the input spectral radiance data at 1,020 ℃. Here, the input spectral radiance data was acquired by multiplying the blackbody spectral radiance values derived from Planck's law at 1,020 ℃ (shown in Figure 4.15) by the emissivity value 0.95. The generated function uses the spectral radiance ($W \cdot m^{-3} \cdot sr^{-1}$), the wavelength (nm), and the emissivity at the selected wavelength as an input. The function derives the temperature using a numerical method to find the temperature that matches the given spectral radiance value. Here, λ_2 was 665.678 nm. Figure 4.16 shows an image of the function that was used to derive the temperature of the recovered spectrum. It turned out that the temperature of the recovered spectrum was 1,042.8 ℃.

After the temperature was calculated using the function based on Planck's law, the 2D temperature map was yielded by multiplying the normalized third peak image by the temperature that was calculated in the previous step. Figure 4.17 shows the acquired 2D temperature map when the slit is 40 μm open. The third peak cannot be used to calculate the temperature since all the peak data were normalized by the third peak value and the third peak normalized value matches up with the 1,020 ℃ ground truth data. Instead, the second peak value was used to calculate the temperature of the recovered spectral data. For the subsequent experiments, the same method will be used to calculate the temperature of the recovered spectrum and to acquire the 2D temperature map.

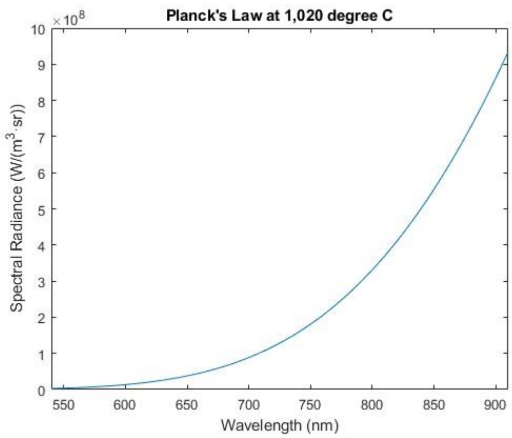

Figure 4.15 Planck’s law at 1,020 °C.

```
function temperature = planck_temperature_graybody(intensity, wavelength, emissivity)
    % Constants
    h = 6.626e-34;  % Planck's constant in J*s
    c = 3.00e8;     % Speed of light in m/s
    k = 1.38e-23;   % Boltzmann constant in J/K

    % Convert wavelength from nm to meters
    wavelength_m = wavelength * 1e-9;

    % Define a function to compute intensity given temperature
    planck_intensity = @(T) (2 * h * c^2)*emissivity / (wavelength_m^5 * (exp((h * c) / (wavelength_m * k * T)) - 1));

    % Use numerical methods to find temperature that matches given intensity
    temperature = fzero(@(T) planck_intensity(T) - intensity, 600); % Start with an initial guess of 600
end
```

Figure 4.16 MATLAB function used to derive the temperature of the recovered spectrum.

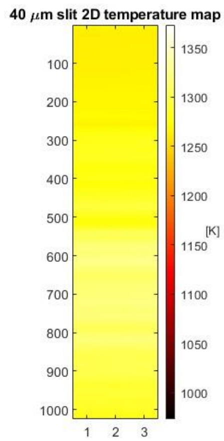

Figure 4.17 Acquired 2D temperature map when the slit width is 40 μm.

4.5 Acquiring a 2D Temperature Map Using HSIS at a 3.02 mm Slit

The hyperspectral reconstruction was done by using the CHAIR code. The CHAIR code reconstructed a 2D image and a 1D spectrum simultaneously by generating a 3D cube that has three axes (x, y, λ). The ground truth images were taken when the spectrometer center wavelength was 0 nm, and the camera exposure time was 5 ms. The ground truth image of an oxidized steel rod is shown in Figure 4.18 and the reconstructed image of a selected wavelength (λ_3) is shown in Figure 4.19. The image was normalized by its maximum intensity value of the λ_3 reconstructed image.

The reconstructed spectrum for each selected wavelength (λ_1, λ_2, and λ_3) is shown in Figure 4.20. The 40 μm slit recovery data seems to be more accurate than the 3.02 mm slit recovery data because there is a trade-off between the field of view of the reconstructed image and the quality of the recovered spectral data. The more the spectrometer slit is wider, the more information can be imaged by a single shot, but the spectral data precision would be reduced since the spectrometer slit is wider.

Similar to the 40 μm slit data, the ratio (R) of the second peak value of the normalized recovered spectral data to the second peak value of the normalized ground truth data was calculated. Equation (4.2) shows the R value for the 3.02 mm slit width.

$$R_{3.02\ mm\ slit} = \frac{Normalized\ recovered\ value_{\lambda_2}}{Normalized\ ground\ truth\ value_{\lambda_2}} = \frac{0.0476329}{0.140518} \qquad (4.2)$$

The temperature of the recovered spectrum was derived using the function based on Planck's law and it was 951.03 ℃. Figure 4.21 shows the acquired 2D temperature map when the spectrometer slit was 3.02 mm open.

4.6 Discussion

The recovered spectrum temperature was 1,042.8 ℃ and 951.03 ℃ for the 40 μm slit, and the 3.02 mm slit, respectively. Each case showed an error rate of 2.24 % and 6.76 %. Figure 4.22 shows the two recovered spectra plotted together with the ground truth data. The position of the recovered spectrum was determined based on the unmodulated spectrum acquired simultaneously during the experiment.

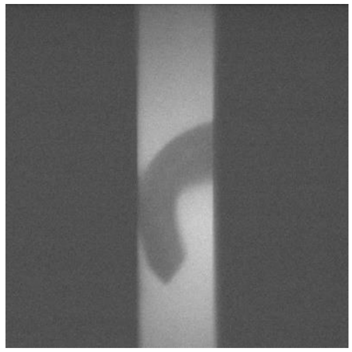

Figure 4.18 Ground truth image of 3.02 mm slit (oxidized steel rod).

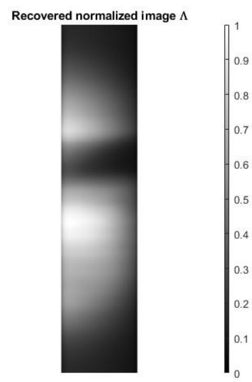

Figure 4.19 Reconstructed image of 3.02 mm slit.

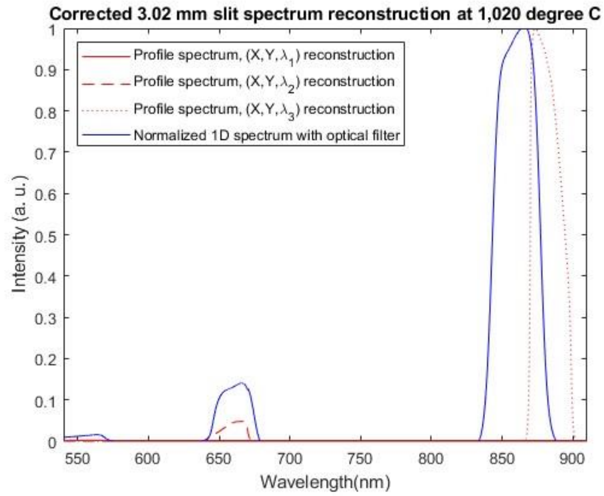

Figure 4.20 Reconstructed spectrum of 3.02 mm slit.

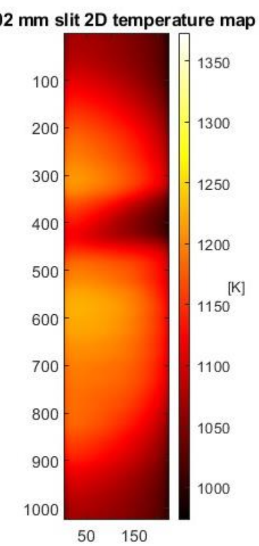

Figure 4.21 The 2D temperature map of a 3.20 mm slit.

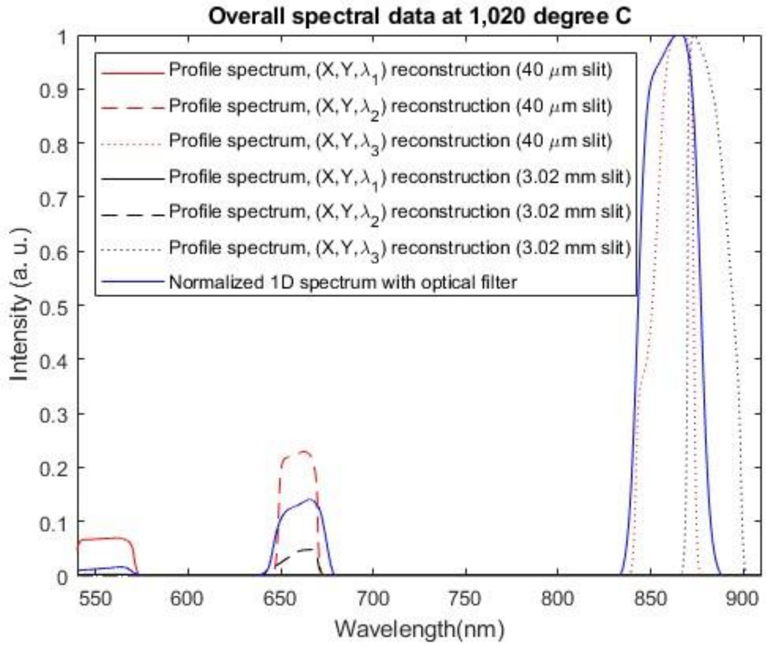

Figure 4.22 Recovered spectral data of both slit sizes.

There are three aspects that the proposed hyperspectral imaging system can improve. The first is about the recovered spatial data. The experiment that used a green and red laser proved the 2D spatial data reconstruction capability of the system. However, in the final experiment acquiring the 2D temperature map, the CHAIR algorithm was not able to reconstruct the 2D spatial data properly. Since a steel rod with an oxidized surface was positioned a couple of millimeters away from the graphite plate to be captured by the imaging system, this could have impacted the results. Multiple attempts were made to attach materials or engrave a pattern on the graphite plate surface but all of them did not work since the graphite plate was heated to a high temperature. As the plate was heated, the surface melted, and the attached materials or engravings disappeared as the experiment proceeded. A different method should be used for future experiments. Moreover, overlaps occurred due to neighboring emissions and made the spectrum appear as a continuum. As a result, the modulation pattern was blurred and the ability to recover the spatial details was hindered. Figure 4.23 shows the modulated image when the spectrometer center wavelength was set to 605 nm. The modulation pattern is blurred, and the pattern is imaged as lines instead of dots. This is the fundamental limit of the current setup. One alternative is to use a back-illuminated LCD to produce the pattern on the structure. This would prevent the superimposition of the patterns and improve the quality of the recovered spatial data.

The second is about the recovered spectral data. It turned out that the recovered spectral data is narrower than the ground truth data because there is an inherent loss whenever the algorithm attempts to recover data. This is related to how the CHAIR algorithm operates. The TwIST algorithm that is included in the CHAIR algorithm consists of two parts that are convergence and denoising. To recover the data to its full extent, both parts of the TwIST algorithm should be revised. To increase the accuracy of the recovered spectral data, a correction factor can be applied to decrease the discrepancy between the ground truth data and the recovered data. The correction factor should be derived by obtaining data in different temperatures and wavelengths. Also, acquiring data by varying the grating groove frequency and blaze and finding the best grating setting for the current experimental setup is recommended.

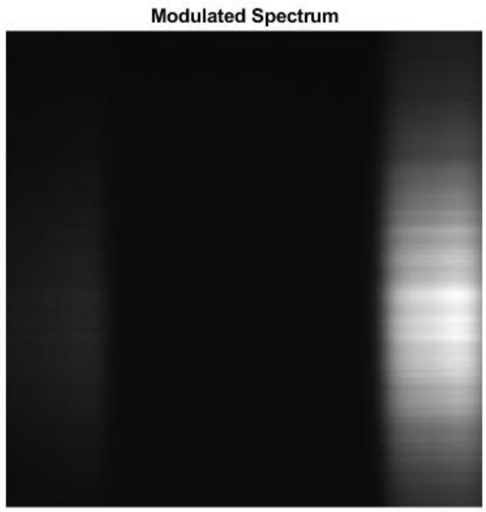

Figure 4.23 Modulated image showing that the modulation pattern is blurred.

The third is about emissivity. Instead of simply assuming the target material is a graybody with an emissivity value of 0.95, the actual emissivity can be calculated by dividing the normalized ground truth data by the normalized Planck's law data for every single data point. Figure 4.24 is a diagram that shows how emissivity can be obtained. To describe the large and small errors that were present during data acquisition, uncertainty should be considered. There were some factors that contributed to uncertainty and the major source of uncertainty was determined as the superimposition of the binary patterns due to the neighboring emissions. Since the binary pattern is blurred due to the overlay of the neighboring emissions, the algorithm was not able to clearly identify the pattern in the slices of the cube. The errors occurred when the algorithm attempted to scan the cube slices with the binary pattern image to remove the residuals of the coding pattern.

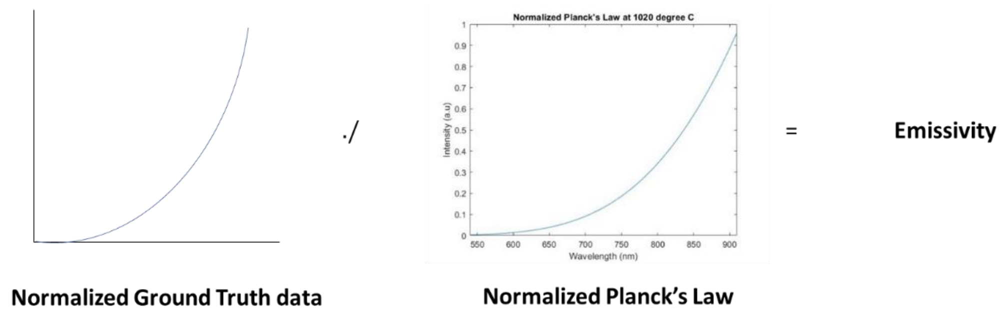

Figure 4.24 Emissivity calculation.

CHAPTER FIVE
CONCLUSIONS AND RECOMMENDATIONS

Conclusions and Future Work

A hyperspectral imaging system has been developed to acquire a 2D temperature map of a graphite plate. The designed system is advantageous since a 2D temperature map can be acquired by a single shot. The acquired spatial and spectral data were formed into a 3D cube (x,y,λ) and were reconstructed as a compressed hyperspectral image that carries wavelength spectra at any pixel in the 2D spatial images at certain wavelengths. Planck's law was applied to calculate the temperature of the pixels in the hyperspectral image. The reconstructed spectral data having different spectrometer slit sizes (40 μm and 3.02 mm) showed that there is a trade-off between the spectral data quality and the field of view of the reconstructed image (spatial data) depending on the spectrometer slit width. By assuming that the graphite is a graybody that has an emissivity value of 0.95, the temperature of the recovered spectral data for the 40 μm slit and the 3.02 mm slit were 1042.8 ℃ and 951.03 ℃, respectively and the error rate was 2.24 % for the 40 μm slit, and 6.76 % for the 3.02 mm slit. It is remarkable that a 2D temperature map was obtained by using the CHAIR algorithm for the first time and the actual implementation will be possible in the fields of thermography, combustion, and other diagnostics. Also, adding more channels to the current experimental setup that varies in the optical path length would make it feasible to acquire data of a target that has a changing temperature. The frame rate of the imaging system could be readily adjusted by setting the optical path length to the desired value.

As aforementioned, the major source of uncertainty was determined as the superimposition of the binary patterns due to the neighboring emissions. To reduce the discrepancy between the recovered results and the ground truth data, it is highly recommended to use a different method that could prevent the pattern from superimposing when it is imaged by the system. The most recommended solution is to use a back-illuminated LCD to produce the pattern on the structure. Applying this method would solve the problem and make this a more reliable imaging system.

LIST OF REFERENCES

[1] Baehr, H. D., and Stephan, K., "Heat and Mass Transfer," Springer Berlin Heidelberg, Berlin, Heidelberg, 2011. https://doi.org/10.1007/978-3-642-20021-2

[2] Goetz, Alexande. F. H., and Srivastava, V., "MINERALOGICAL MAPPING IN THE CUPRITE MINING DISTRICT, NEVADA."

[3] Lowe, D. S., Wilson, C. L., and Arbor, A., "MULTISPECTRAL SCANNING SYSTEMS: THEIR FEATURES AND LIMITATIONS."

[4] Engle, J. L., and Weinstein, O., "The Thematic Mapper---An Overview," *IEEE Transactions on Geoscience and Remote Sensing*, Vol. GE-21, No. 3, 1983, pp. 258–265. https://doi.org/10.1109/TGRS.1983.350551

[5] Khan, M. J., Khan, H. S., Yousaf, A., Khurshid, K., and Abbas, A., "Modern Trends in Hyperspectral Image Analysis: A Review," *IEEE Access*, Vol. 6, 2018, pp. 14118–14129. https://doi.org/10.1109/ACCESS.2018.2812999

[6] Pei, Z., Huang, Y. M., and Zhou, T., "Review on Analysis Methods Enabled by Hyperspectral Imaging for Cultural Relic Conservation," *Photonics*, Vol. 10, No. 10, 2023, p. 1104. https://doi.org/10.3390/photonics10101104

[7] Liang, H., "Advances in Multispectral and Hyperspectral Imaging for Archaeology and Art Conservation," *Applied Physics A*, Vol. 106, No. 2, 2012, pp. 309–323. https://doi.org/10.1007/s00339-011-6689-1

[8] Soni, A., Dixit, Y., Reis, M. M., and Brightwell, G., "Hyperspectral Imaging and Machine Learning in Food Microbiology: Developments and Challenges in Detection of Bacterial, Fungal, and Viral Contaminants," *Comprehensive Reviews in Food Science and Food Safety*, Vol. 21, No. 4, 2022, pp. 3717–3745. https://doi.org/10.1111/1541-4337.12983

[9] Mariotti, K. D. C., Ortiz, R. S., and Ferrão, M. F., "Hyperspectral Imaging in Forensic Science: An Overview of Major Application Areas," *Science & Justice*, Vol. 63, No. 3, 2023, pp. 387–395. https://doi.org/10.1016/j.scijus.2023.04.003

[10] Wu, Y., Xu, Z., Yang, W., Ning, Z., and Dong, H., "Review on the Application of Hyperspectral Imaging Technology of the Exposed Cortex in Cerebral Surgery," *Frontiers in Bioengineering and Biotechnology*, Vol. 10, 2022, p. 906728. https://doi.org/10.3389/fbioe.2022.906728

[11] Ferrari, C., Foca, G., and Ulrici, A., "Handling Large Datasets of Hyperspectral Images: Reducing Data Size without Loss of Useful Information," *Analytica Chimica Acta*, Vol. 802, 2013, pp. 29–39. https://doi.org/10.1016/j.aca.2013.10.009

[12] Wong, K.-K., "Development of Co-Boresighted Vis-NIR-SWIR Hyperspectral Imaging Systems," presented at the SPIE Sensing Technology + Applications, Baltimore, Maryland, USA, 2014. https://doi.org/10.1117/12.2055490

[13] Harms, J. D., Bachmann, C. M., Faulring, J. W., and Ruiz Torres, A. J., "A next Generation Field-Portable Goniometer System," presented at the SPIE Defense + Security, Baltimore, Maryland, United States, 2016. https://doi.org/10.1117/12.2223180

[14] Furukawa, T., "Detecting Indentations on Documents Pressed by Pen Tip Force Using a Near Infrared Light Emitting Diode (NIR LED) and Shape from Shading," Berlin, Heidelberg, 2011.

[15] Misra, N. N., Dixit, Y., Al-Mallahi, A., Bhullar, M. S., Upadhyay, R., and Martynenko, A., "IoT, Big Data, and Artificial Intelligence in Agriculture and Food Industry," *IEEE Internet of Things Journal,* Vol. 9, No. 9, 2022, pp. 6305–6324. https://doi.org/10.1109/JIOT.2020.2998584

[16] Khan, A., Vibhute, A. D., Mali, S., and Patil, C. H., "A Systematic Review on Hyperspectral Imaging Technology with a Machine and Deep Learning Methodology for Agricultural Applications," *Ecological Informatics,* Vol. 69, 2022, p. 101678. https://doi.org/10.1016/j.ecoinf.2022.101678

[17] School of Natural Sciences, Department of Electrical and Electronics Engineering Bolu Abant Izzet Baysal University, 14280, Bolu, Turkey, Ozdemir, A., Polat, K., and Department of Electrical and Electronics Engineering, Faculty of Engineering, Bolu Abant Izzet Baysal University, 14280, Bolu, Turkey, "Deep Learning Applications for Hyperspectral Imaging: A Systematic Review," *Journal of the Institute of Electronics and Computer*, Vol. 2, No. 1, 2020, pp. 39–56. https://doi.org/10.33969/JIEC.2020.21004

[18] Urbanos, G., Martín, A., Vázquez, G., Villanueva, M., Villa, M., Jimenez-Roldan, L., Chavarrías, M., Lagares, A., Juárez, E., and Sanz, C., "Supervised Machine Learning Methods and Hyperspectral Imaging Techniques Jointly Applied for Brain Cancer Classification," *Sensors,* Vol. 21, No. 11, 2021, p. 3827. https://doi.org/10.3390/s21113827

[19] Sharma, V., and Kumar, R., "Trends of Chemometrics in Bloodstain Investigations," *TrAC Trends in Analytical Chemistry,* Vol. 107, 2018, pp. 181–195. https://doi.org/10.1016/j.trac.2018.08.006

[20] Edelman, G., Van Leeuwen, T. G., and Aalders, M. C. G., "Hyperspectral Imaging for the Age Estimation of Blood Stains at the Crime Scene," *Forensic Science International*, Vol. 223, Nos. 1–3, 2012, pp. 72–77. https://doi.org/10.1016/j.forsciint.2012.08.003

[21] Cadd, S., Li, B., Beveridge, P., O'Hare, W. T., Campbell, A., and Islam, M., "The Non-Contact Detection and Identification of Blood Stained Fingerprints Using Visible Wavelength Reflectance Hyperspectral Imaging: Part 1," *Science & Justice,* Vol. 56, No. 3, 2016, pp. 181–190. https://doi.org/10.1016/j.scijus.2016.01.004

[22] Cadd, S., Li, B., Beveridge, P., O'Hare, W. T., Campbell, A., and Islam, M., "The Non-Contact Detection and Identification of Blood Stained Fingerprints Using Visible Wavelength Hyperspectral Imaging: Part II Effectiveness on a Range of Substrates," *Science & Justice*, Vol. 56, No. 3, 2016, pp. 191–200. https://doi.org/10.1016/j.scijus.2016.01.005

[23] Schuler, R. L., Kish, P. E., and Plese, C. A., "Preliminary Observations on the Ability of Hyperspectral Imaging to Provide Detection and Visualization of Bloodstain Patterns on Black Fabrics," *Journal of Forensic Sciences*, Vol. 57, No. 6, 2012, pp. 1562–1569. https://doi.org/10.1111/j.1556-4029.2012.02171.x

[24] Li, B., Beveridge, P., O'Hare, W. T., and Islam, M., "The Application of Visible Wavelength Reflectance Hyperspectral Imaging for the Detection and Identification of Blood Stains," *Science & Justice*, Vol. 54, No. 6, 2014, pp. 432–438. https://doi.org/10.1016/j.scijus.2014.05.003

[25] Fabelo, H., Halicek, M., Ortega, S., Shahedi, M., Szolna, A., Piñeiro, J., Sosa, C., O'Shanahan, A., Bisshopp, S., Espino, C., Márquez, M., Hernández, M., Carrera, D., Morera, J., Callico, G., Sarmiento, R., and Fei, B., "Deep Learning-Based Framework for In Vivo Identification of Glioblastoma Tumor Using Hyperspectral Images of Human Brain," *Sensors*, Vol. 19, No. 4, 2019, p. 920. https://doi.org/10.3390/s19040920

[26] Manni, F., Van Der Sommen, F., Fabelo, H., Zinger, S., Shan, C., Edström, E., Elmi-Terander, A., Ortega, S., Marrero Callicó, G., and De With, P. H. N., "Hyperspectral Imaging for Glioblastoma Surgery: Improving Tumor Identification Using a Deep Spectral-Spatial Approach," *Sensors*, Vol. 20, No. 23, 2020, p. 6955. https://doi.org/10.3390/s20236955

[27] Mori, M., Chiba, T., Nakamizo, A., Kumashiro, R., Murata, M., Akahoshi, T., Tomikawa, M., Kikkawa, Y., Yoshimoto, K., Mizoguchi, M., Sasaki, T., and Hashizume, M., "Intraoperative Visualization of Cerebral Oxygenation Using Hyperspectral Image Data: A Two-Dimensional Mapping Method," *International Journal of Computer Assisted Radiology and Surgery*, Vol. 9, No. 6, 2014, pp. 1059–1072. https://doi.org/10.1007/s11548-014-0989-9

[28] Iwaki, K., Takagishi, S., Arimura, K., Murata, M., Chiba, T., Nishimura, A., Ren, N., and Iihara, K., "A Novel Hyperspectral Imaging System for Intraoperative Prediction of Cerebral Hyperperfusion Syndrome after Superficial Temporal Artery-Middle Cerebral Artery Anastomosis in Patients with Moyamoya Disease," *Cerebrovascular Diseases*, Vol. 50, No. 2, 2021, pp. 208–215. https://doi.org/10.1159/000513289

[29] Nguyen, T. N., Wu, W., Woldemichael, E., Toronov, V., and Lin, S., "Hyperspectral Near-Infrared Spectroscopy Assessment of the Brain during Hypoperfusion," *Journal of Biomedical Optics*, Vol. 24, No. 03, 2019, p. 1. https://doi.org/10.1117/1.JBO.24.3.035007

[30] Nosrati, R., Vesely, K., Schweizer, T. A., and Toronov, V., "Event-Related Changes of the Prefrontal Cortex Oxygen Delivery and Metabolism during Driving Measured by Hyperspectral fNIRS," *Biomedical Optics Express*, Vol. 7, No. 4, 2016, p. 1323. https://doi.org/10.1364/BOE.7.001323

[31] Fabelo, H., Ortega, S., Szolna, A., Bulters, D., Pineiro, J. F., Kabwama, S., J-O'Shanahan, A., Bulstrode, H., Bisshopp, S., Kiran, B. R., Ravi, D., Lazcano, R., Madronal, D., Sosa, C., Espino, C., Marquez, M., De La Luz Plaza, M., Camacho, R., Carrera, D., Hernandez, M., Callico, G. M., Morera Molina, J., Stanciulescu, B., Yang, G.-Z., Salvador Perea, R., Juarez, E., Sanz, C., and Sarmiento, R., "*In-Vivo* Hyperspectral Human Brain Image Database for Brain Cancer Detection," *IEEE Access*, Vol. 7, 2019, pp. 39098–39116. https://doi.org/10.1109/ACCESS.2019.2904788

[32] Hao, Q., Pei, Y., Zhou, R., Sun, B., Sun, J., Li, S., and Kang, X., "Fusing Multiple Deep Models for *In Vivo* Human Brain Hyperspectral Image Classification to Identify Glioblastoma Tumor," *IEEE Transactions on Instrumentation and Measurement*, Vol. 70, 2021, pp. 1–14. https://doi.org/10.1109/TIM.2021.3117634

[33] Devesse, W., De Baere, D., and Guillaume, P., “High Resolution Temperature Measurement of Liquid Stainless Steel Using Hyperspectral Imaging,” *Sensors*, Vol. 17, No. 1, 2017, p. 91. https://doi.org/10.3390/s17010091

[34] Medina, J. S., Devesse, W., Ertveldt, J., and Guillaume, P., “Comparison of Visual and Hyperspectral Monitoring of the Melt Pool during Laser Metal Deposition,” *Procedia CIRP*, Vol. 94, 2020, pp. 462–468. https://doi.org/10.1016/j.procir.2020.09.165

[35] Otsu, N., “A Threshold Selection Method from Gray-Level Histograms,” *IEEE Transactions on Systems, Man, and Cybernetics*, Vol. 9, No. 1, 1979, pp. 62–66. https://doi.org/10.1109/TSMC.1979.4310076

[36] Myers, A. J., Quirarte, G., Ogoke, F., Lane, B. M., Uddin, S. Z., Farimani, A. B., Beuth, J. L., and Malen, J. A., “High-Resolution Melt Pool Thermal Imaging for Metals Additive Manufacturing Using the Two-Color Method with a Color Camera,” *Additive Manufacturing*, Vol. 73, 2023, p. 103663. https://doi.org/10.1016/j.addma.2023.103663

[37] Gorevoy, A., Machikhin, A., Bykov, A., and Kren, A., “Optimization of Data Acquisition Algorithm for Temperature and Emissivity Distribution Measurement Using Snapshot Hyperspectral Imaging Systems,” *Case Studies in Thermal Engineering*, Vol. 26, 2021, p. 101154. https://doi.org/10.1016/j.csite.2021.101154

[38] Jørgensen, A. L., Larsen, M. N., Petrunin, V., Kjelstrup-Hansen, J., and Jørgensen, B., “Surface Temperature Determination Using Long Range Thermal Emission Spectroscopy Based on a First Order Scanning Fabry-Pérot Interferometer,” *Optics Express*, Vol. 30, No. 2, 2022, p. 2186. https://doi.org/10.1364/OE.441798

[39] Pan, G., Li, B., Gu, G., Yu, X., Li, H., Wang, X., Li, Z., Yang, X., Zhu, J., Cao, D., Li, B., Ma, Q., Wu, H., He, L., and Lin, G., “Analysis of the Impact of Temperature on the Spectral Shift in Ultraviolet Hyperspectral Imaging Spectrometers,” *Optics Express*, Vol. 32, No. 7, 2024, p. 11774. https://doi.org/10.1364/OE.517945

[40] He, Z., Williamson, N., Smith, C. D., Gragston, M., and Zhang, Z., “Compressed Single-Shot Hyperspectral Imaging for Combustion Diagnostics,” *Applied Optics*, Vol. 59, No. 17, 2020, p. 5226. https://doi.org/10.1364/AO.390335

[41] Bioucas-Dias, J. M., and Figueiredo, M. A. T., “A New TwIST: Two-Step Iterative Shrinkage/Thresholding Algorithms for Image Restoration,” *IEEE Transactions on Image Processing*, Vol. 16, No. 12, 2007, pp. 2992–3004. https://doi.org/10.1109/TIP.2007.909319

VITA

Anthony Kim was born in Knoxville, Tennessee. After graduating from Hongik University, Korea in 2022 with a Bachelor of Science in Mechanical Engineering, he worked as a researcher at the Korea Textile Machinery Convergence Research Institute developing industrial robot systems for textile manufacturing. He enrolled in the Master's Mechanical Engineering program at The University of Tennessee in Knoxville in the Fall 2022 semester. His research is focused on hyperspectral imaging and digital image processing.